

This is the peer reviewed version of the following article:

Ductile-brittle deformation effects on crystal-chemistry and U-Pb ages of magmatic and metasomatic zircons from a dyke of the Finero Mafic Complex (Ivrea-Verbano Zone, Italian Alps) / Langone, Antonio; Padrón Navarta José, Alberto; Ji, Wei Qiang; Zanetti, Alberto; Mazzucchelli, Maurizio; Tiepolo, Massimo; Giovanardi, Tommaso; Bonazzi, Mattia. - In: LITHOS. - ISSN 0024-4937. - 284-285:(2017), pp. 493-511. [10.1016/j.lithos.2017.04.020]

Terms of use:

The terms and conditions for the reuse of this version of the manuscript are specified in the publishing policy. For all terms of use and more information see the publisher's website.

10/04/2024 07:41

Accepted Manuscript

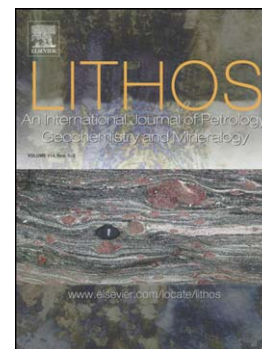
Ductile-brittle deformation effects on crystal-chemistry and U–Pb ages of magmatic and metasomatic zircons from a dyke of the Finero Mafic Complex (Ivrea-Verbano Zone, Italian Alps)

Langone Antonio, Padrón-Navarta José Alberto, Ji Wei-Qiang, Zanetti Alberto, Mazzucchelli Maurizio, Tiepolo Massimo, Tommaso Giovanardi, Mattia Bonazzi

PII: S0024-4937(17)30169-X
DOI: doi:[10.1016/j.lithos.2017.04.020](https://doi.org/10.1016/j.lithos.2017.04.020)
Reference: LITHOS 4302

To appear in: *LITHOS*

Received date: 11 November 2016
Accepted date: 22 April 2017



Please cite this article as: Antonio, Langone, Alberto, Padrón-Navarta José, Wei-Qiang, Ji, Alberto, Zanetti, Maurizio, Mazzucchelli, Massimo, Tiepolo, Giovanardi, Tommaso, Bonazzi, Mattia, Ductile-brittle deformation effects on crystal-chemistry and U–Pb ages of magmatic and metasomatic zircons from a dyke of the Finero Mafic Complex (Ivrea-Verbano Zone, Italian Alps), *LITHOS* (2017), doi:[10.1016/j.lithos.2017.04.020](https://doi.org/10.1016/j.lithos.2017.04.020)

This is a PDF file of an unedited manuscript that has been accepted for publication. As a service to our customers we are providing this early version of the manuscript. The manuscript will undergo copyediting, typesetting, and review of the resulting proof before it is published in its final form. Please note that during the production process errors may be discovered which could affect the content, and all legal disclaimers that apply to the journal pertain.

Ductile-brittle deformation effects on crystal-chemistry and U-Pb ages of magmatic and metasomatic zircons from a dyke of the Finero Mafic Complex (Ivrea-Verbano Zone, Italian Alps)

Langone Antonio¹, Padrón-Navarta José Alberto², Ji Wei-Qiang³, Zanetti Alberto¹, Mazzucchelli Maurizio^{4,1}, Tiepolo Massimo^{5,1}, Tommaso Giovanardi⁶, Mattia Bonazzi⁷

1 Istituto di Geoscienze e Georisorse-C.N.R. U.O.S. of Pavia, Via Ferrata 1, 27100 Pavia, Italy

2 Géosciences Montpellier, CNRS - Univ. Montpellier, 34095 Montpellier, France

3 State Key Laboratory of Lithospheric Evolution, Institute of Geology and Geophysics, Chinese Academy of Sciences, PO Box 9825, 100029 Beijing, China

4 Dipartimento di Scienze Chimiche e Geologiche, Università degli Studi di Modena e Reggio Emilia, Via Campi, 103 I-41125 Modena, Italy

5 Dipartimento di Scienze della Terra “A. Desio”, Università degli Studi di Milano, Via Botticelli 23, Milano, Italy

6 Instituto de Geociências, Universidade de São Paulo, Rua do Lago, 562, Cidade Universitária, 05508-900 São Paulo, Brazil

7 Dipartimento di Scienze della Terra e dell’Ambiente, Università di Pavia, Via Ferrata 1, 27100 Pavia

Abstract

A detailed microstructural, geochemical and geochronological study was performed on zircon grains from plagioclase-rich dioritic dykes discordantly intruded within meta-diorites/gabbros forming the External Gabbro unit of the Finero Mafic Complex (Italian Alps). This unit is exposed as part of a near complete crustal section spanning from mantle

rocks to upper crustal metasediments (Val Cannobina, Ivrea-Verbano Zone, Italy). The leucocratic dykes consist mainly of plagioclase ($An_{18-24}Ab_{79-82}Or_{0.3-0.7}$) with subordinate amounts of biotite and spinel defining melanocratic layers. Zircon and corundum are common accessory phases. Both the dykes and the surrounding meta-diorites/gabbros show evidence of ductile deformation under amphibolite-facies conditions.

Zircon grains/fragments (up to 2 mm in length) occur as porphyroclasts surrounded by fine-grained plagioclase within the leucocratic domains and may occur within the melanocratic layers completely or partially surrounded by biotite and spinels. Fractures are common within zircon, define networks and have associated displacements occasionally and/or they can be filled by secondary minerals.

Cathodoluminescence (CL) images reveal that zircon grains from the leucocratic layers show relicts of primary magmatic (i.e. oscillatory and or sector) zoning generally related with the crystal shapes or crystallographic orientation, whereas those from the melanocratic domains does not. In both cases, zircon shows secondary CL features, i.e. mosaic-like textures, due to deformation. EBSD maps confirmed a profuse mosaic texture, resulting in an internal misorientation of ca. 10° , generally associated with fractures.

Locally, zircon shows clear evidence of crystal-plastic deformation at the edges, with a gradual misorientations of up to 12° , suggesting an origin prior fragmentation.

Trace elements and U–Pb analyses were carried out by LA-ICP-MS directly on petrographic thin sections. Such *in situ* investigations revealed a strong correlation between internal zircon structures, chemistry, U–Pb isotope ratios and mylonitic fabric.

U-Pb data return highly discordant and variable ages. The $^{206}Pb/^{238}U$ ages may range from ca. 297 to 198 Ma within the same zircon grain from the leucocratic layers, whereas $^{206}Pb/^{238}U$ younger than 250 Ma were systematically obtained from zircon within the melanocratic layers. The $^{206}Pb/^{238}U$ data younger than ca. 240 Ma from zircon grains within the leucocratic layers were obtained from narrow axial stripes observed in CL

images and oriented parallel or at low-angle with respect to the foliation planes. These stripes are characterized by an overall HREE, Y, U and Th enrichment possibly reflecting deformation of the grain in presence of interstitial fluid phases. Combining U-Pb data, microstructure and zircon CL features, we suggest a multistage evolution of the dykes whereby the melanocratic layers are the result of a Late Permian metasomatic event promoting modification of the pre-existing mineral assemblage of the (Late Carboniferous–Early Permian?) dykes and deformation and partial resetting of zircon porphyroclasts. This has important implications in the geology of the Ivrea-Verbano Zone because, having the dyke intruded the External Gabbro unit before Triassic (probably during Carboniferous–Permian), the latter cannot be considered a Triassic intrusion. At least part of the External Gabbro unit is Carboniferous–Permian as the other mafic bodies of the Ivrea-Verbano Zone.

Keywords

Microstructures

Zircon

U-Pb dating

Trace elements

Mafic dyke

Ivrea-Verbano Zone

1. Introduction

The Ivrea–Verbano Zone (IVZ, Southern Alps, Italy–Switzerland) consists of a worldwide unique section of lower continental crust. This crustal section has attracted a significant attention as it represents a natural laboratory to study magmatic and metamorphic processes at lower crustal levels. At present, one of the most debated topic

is the timing of under- and intra-plating of mafic melts at lower crustal level being essentially Early Permian in the central part of the IVZ (i.e., Sesia and Sessera Valleys, (Quick et al., 1995, 2009; Sinigoi et al., 1996, 2011; Peressini et al., 2007, Mazzucchelli et al., 2014) and Middle Triassic in the northeastern sector (i.e., Finero, Zanetti et al., 2013). In the latter, there are further evidences of the occurrence of widespread Triassic magmatism consisting mainly of late alkaline veins and pockets (e.g., zircon-bearing diorites and nepheline diorite pegmatites) mostly showing Late Triassic to Early Jurassic ages (Stähle et al., 1990, 2001; Oppizzi and Schaltegger, 1999; Grieco et al., 2001; Klötzli et al., 2007, 2009; Schaltegger et al., 2015, and references therein). Determine accurate emplacement ages of later dykes and sills is pivotal in constraining the magmatic evolution of large igneous bodies because they provide excellent regional time markers and may be associated to major geodynamic process (e.g. French and Heaman, 2010).

In this study, zircon grains from dioritic dykes (plagioclase, biotite, zircon, corundum and epidote) cutting the main magmatic body (i.e., the External Gabbro unit) of the northeastern sector of the IVZ were examined in order to shed light on the magmatic evolution. Despite the common occurrence of zircon and its robustness as geochronometer (e.g. Harley and Kelly, 2007) a precise U–Pb dating of this late magmatic products resulted difficult due to common occurrence of discordant and highly variable U–Pb data.

Experimental studies indicate that, with the exception of extremely high temperature conditions, zircon is characterized by low diffusion rates, which can be significant only at extreme high temperature (e.g. Cherniak and Watson, 2003). However, it has been largely documented that diffusion at lower temperatures can be enhanced by annealing of metamictic domains (e.g. Geisler et al., 2001) and by brittle and crystal-plastic deformation (e.g. Timms et al., 2006). Moreover, recent research has indicated that crystal-plastic deformation can dramatically affect the trace element distribution and isotopic composition

of the whole or portions of the zircon grain suggesting that zircon may not be as chemically robust as once believed (e.g., Reddy et al., 2006; Timms et al., 2006; 2011; 2017; Rimša et al., 2007; MacDonald et al., 2013; Kovaleva et al., 2014; Peterman et al., 2016; Piazzolo et al., 2012, 2016; Reddy et al., 2016; La Fontaine et al., 2017; Tretriakova et al., 2017). Deformation microstructures and related chemical changes are generally masked in optical microscopy; they may be cryptic also in cathodoluminescence images due to negligible changes to the integrated emission intensity (e.g., Timms and Reddy, 2009); they can be identified in (high-resolution) electron backscattered diffraction (EBSD) maps. Measuring the chemical variations associated with deformation microstructures at the micron, sub-micron and atomic scale is a challenge as the spatial resolution of conventional *in situ* techniques such as SHRIMP and LA-(MC)-ICP-MS, currently used for geochronological and geochemical studies, is in the range of 5-15 μ m and 15-50 μ m, respectively (La Fontaine et al., 2017). The recent applications of atom probe microscopy to zircon have highlighted the potential of this analytical technique to quantify nanoscale compositional variation (e.g. Valley et al., 2014; 2015; Peterman et al., 2016; Reddy et al., 2016; Piazzolo et al., 2016; La Fontaine et al., 2017).

Taking into account these limitations due to the crystal plastic-deformation of zircon and the spatial resolution we characterized the microstructural features by electron backscattered diffraction (EBSD) of selected zircon grains. We performed *in situ* LA-ICP-MS U–Pb dating, trace element composition and Hf isotopes of zircon grains directly on thin section in order to observe the influence of microstructural fabrics, such as orientation of foliation planes and grain size of the surrounding mylonitic matrix, on both chemical and isotopic data. This approach allowed us to constrain a multistage evolution of the studied dyke with a crystallization event followed by metasomatism coeval with brittle-ductile deformation.

2. Geological setting and geochronological background

The IVZ represents an uplifted part of the pre–Alpine intermediate–lower continental crust located in the Southern Alps of northwest Italy (e.g. Schmid, 1993). The northernmost sector of the IVZ (Fig. 1A) is characterized by mantle peridotites (the Phlogopite Peridotite), intrusive crustal mafic to ultramafic rocks, the so-called Finero Mafic Complex, and supracrustal metamorphic rocks (the Kinzigite Formation).

The Finero Mafic Complex consists of three different units (Siena and Coltorti, 1989): i) the Layered Internal Zone (garnet–hornblende, pyroxenites, anorthosites and garnet–gabbros), in contact with the mantle Phlogopite Peridotite; ii) the Amphibole Peridotite and iii) the External Gabbro, which is in contact with the Kinzigite Formation (Fig. 1A, B). The External Gabbro unit is 400–500 m thick and consists of metabasites derived mainly from amphibole gabbro and diorite and in minor extent from pyroxenite and anorthosite bands. Mafic rocks experienced a metamorphic overprint under granulite/amphibolite facies conditions. Several slivers or lenses (<1 m to 100 m thick) of granulites from lithologies of the Kinzigite Formation occur within the External Gabbro unit and are referred as septa (Fig. 1B, Hingerl et al., 2008; Mazzucchelli et al., 2014; Langone & Tiepolo, 2015). The External Gabbro unit is bounded by two shear zones, which mark the contact with the adjacent Amphibole Peridotite unit and the Kinzigite Formation (Fig. 1B; Kenkmann 2000, Langone & Tiepolo 2015). In the Val Cannobina area, the rocks of the External Gabbro unit, the septa and the metamorphic rocks of the Kinzigite Formation, show a marked mylonitic deformation (e.g. Boriani et al. 1990; Langone & Tiepolo 2015).

The whole mafic/ultramafic sequence exposed in the northeastern sector of the IVZ (Fig. 1A, B) is crosscut by late pegmatitic dykes and pods whose intrusion age has been the subject of numerous geochronological studies (e.g. Stähle et al., 1990, 2001; von Quadt et al. 1993; Grieco et al. 2001; Klötzli et al., 2007; Hingerl et al., 2008; Schaltegger et al., 2015). In particular, Stähle et al. (1990) dated zircons from a Na-alkaline dioritic

pegmatitic dyke within the mantle body at 225 ± 13 Ma by the Pb–Pb evaporation technique. Oppizzi & Schaltegger (1999) dated zircon (U–Pb, TIMS) from a plagioclase lens within the gabbro of the Layered Internal Zone, obtaining a weighted mean $^{206}\text{Pb}/^{238}\text{U}$ age of 212.5 ± 0.5 Ma. Grieco et al. (2001) also reported TIMS U–Pb ages of zircon grains of 195 ± 4 Ma ($^{206}\text{Pb}/^{238}\text{U}$) and 202 ± 1 Ma (concordant) for an alkali pegmatite and a pegmatitic plagioclase, respectively from the contact between the Amphibole Peridotite unit and the External Gabbro in the northeastern portion of the complex (Fig. 1A). Recent high-precision CA-ID-TIMS $^{206}\text{Pb}/^{238}\text{U}$ dating of fragments of large zircon grains (up to 9 cm) from highly evolved alkaline melts intruded into the lower units of the Finero Mafic Complex were performed by Schaltegger et al. (2015). These authors dated several fragments of zircon from nepheline diorite pegmatites within the Amphibole Peridotite unit and gabbros of the Layered Internal Zone (Fig. 1A) and suggested an emplacement period between 212.5 and 190 Ma.

The geochronological data from these alkaline dykes and pegmatites suggest a Late Triassic to Early Jurassic magmatic/thermal/hydrothermal activity documented until now for the Mantle Peridotite unit and also for part of the Finero Mafic Complex (i.e. Layered Internal Zone and Amphibole Peridotite unit). Further geochronological evidence of a thermal event from Late Triassic to Early Jurassic were found by several authors from different lithologies and applying different methods. More comprehensive geochronological reviews are provided by Zanetti et al. (2013) and Schaltegger et al. (2015), here we focus on U–Pb zircon ages provided for this sector of the IVZ. In a recent SHRIMP U–Pb zircon dating, Zanetti et al. (2013) measured concordant Middle Triassic (232 ± 3 Ma) U–Pb ages from zircon separated by the External Gabbro unit that they interpreted as the age of intrusion. A range of Triassic–Jurassic ages were also reported by von Quadt et al. (1993) and Grieco et al. (2001) for zircon from chromitite layers and/or pods within Mantle Peridotite. Von Quadt et al. (1993) performed conventional multigrain TIMS dating and

obtained concordant U-Pb age of 204 ± 4 Ma and a lower intercept at 207 ± 5 Ma. Analogous determinations by Grieco et al. (2001) defined an upper intercept age of 208 ± 2 Ma, but revealed the presence of an inherited Pb component that plots, reverse discordant, at ca. 225 Ma. Recently, Zanetti et al. (2016) dated by LA-ICP-MS zircon grains from three chromitite layers segregated in dunite bodies belonging to the Mantle Peridotite and obtained $^{206}\text{Pb}/^{238}\text{U}$ data in the range of 199 ± 3 Ma to 178 ± 2 Ma, but with a pronounced peak age ca. 187 Ma. According to these authors, relevant exception is represented by two zircon grains showing relics of zoning at CL, in which darker cores give Triassic $^{206}\text{Pb}/^{238}\text{U}$ ages of 242 ± 7 Ma and 229 ± 7 Ma, and by a third homogeneous zircon giving 208 ± 3 Ma.

In summary, geochronological data from late magmatic dykes, pegmatites, pods and from host rocks suggest an important thermal perturbation at the Triassic-Jurassic transition. Further Late Triassic - Early Jurassic U-Pb data from zircon, monazite and rutile are becoming increasingly common over the whole Ivrea-Verbano zone (e.g. Ewing et al., 2015 and references therein; Langone and Tiepolo, 2015 and references therein) indicating both primary crystallization and secondary recrystallization events.

3. Analytical techniques and approach

Zircon external and internal features were studied directly on six thin sections (ALB-1A, ALB-1B, ALB-2, ALB-1A_mp, ALB-1B_mp, ALB-2_mp) from three samples. Zircon grains were investigated by Scanning Electron Microscopy (SEM): Back-Scattered Electron (BSE) and Cathodoluminescence (CL) imaging. For selected grains we collected Electron Back-Scattered Diffraction (EBSD) maps at the SEM. Table 1 provide a list of the studied zircon grains and summarize the studied techniques adopted for each grain.

3.1. SEM-EBSD

In order to characterize the internal deformation features of zircon in context of the surrounding microstructure, two selected zircon grains, representative of a fragment and a large crystal, were mapped by EBSD in situ. The Crystal Preferred Orientation (CPO) of zircon, plagioclase, magnetite and other minor phases was measured by indexing of electron backscattered diffraction (EBSD) patterns using the CamScan X500FE CrystalProbe equipped with a Oxford Instruments Nordlys Nano digital CCD camera at Géosciences Montpellier (CNRS-Université de Montpellier 2, France). Low-resolution EBSD maps of the thin section or of the textural site were acquired with a step of 10 μm . The internal features of zircon were characterized by acquiring high-resolution EBSD maps with a step size of 1-1.5 μm . For more analytical detail see Appendix C.

3.2. LA-ICP-MS U–Pb dating and trace element composition

U–Pb dating and trace element characterization with laser ablation ICP-MS were carried out on zircon directly on polished thin section at the CNR–IGG UOS of Pavia with Laser Ablation (LA)–ICP–MS. The system couples an ArF excimer laser microprobe (type GeoLas102 from MicroLas) with a sector field ICP–MS (type Element from ThermoFinnigan). U–Pb analyses were carried out using a spot size of 35 μm a repetition rate of 5Hz and a laser fluence of 8 Jcm^{-2} . For the trace element composition, the ablation system was operated at a 10 Hz repetition rate, 50 μm pit size, with a fluence of c. 9 Jcm^{-2} . More analytical details are reported in Appendix C; results are reported in Table A1 and A2.

Except for a large zircon grain highly fractured and damaged during polishing, LA-ICP-MS U-Pb dating and trace element composition were carried out on two zircon grains from the ALB-1A thin section (Zrc2, Zrc4), two zircon grains from ALB-1A_mp thin section (Zrc2 and Zrc3), and different fragments from a large zircon grain within the ALB-1B_mp thin section (**Table 1**). A small monazite grain along the mylonitic matrix from ALB-2 sample

was also analysed. Discordance was calculated as $[(1 - (^{206}\text{Pb}/^{238}\text{U})_{\text{age}} / (^{207}\text{Pb}/^{235}\text{U})_{\text{age}}) * 100]$ and data were considered discordant for percentage of discordance >2.5 . ISOPLOT/Ex 3.00 software package by Ludwig (2003) was used for U–Pb apparent ages calculations and graphical representations. All data in the text and figures are given with the 2-sigma error.

Different analytical strategies were adopted for the location of the analyses; we tried to avoid macrofractures since it is already well-established that significant chemical changes can occur along visible fractures (e.g., Wayne and Sinha, 1988). LA-ICP-MS spots were arranged in several rows and columns (i.e. Zrc4, ALB-1A) in order to cover as much as possible the available surface; in two orthogonal profiles (Zrc2, ALB-1A) along the main crystallographic axes; or they were located in polygonal domains characterized by different CL features and/or microstructures revealed by EBSD maps. The large number of data available for some zircon grains (e.g. Zrc4 and Zrc2, ALB-1A) allowed the construction of contour maps of the U–Pb ages and/or the trace element distributions. Contour maps were produced by using the software SURFER with the Kriging method and default properties (point Kriging with no drifts and a circular search ellipse).

3.3. Zircon Hf isotopes

In-situ hafnium isotopic compositions of three zircon grains were determined at the State Key Laboratory of Lithospheric Evolution, Institute of Geology and Geophysics of the Chinese Academy of Sciences (Beijing, China), by a Thermo-Finnigan Neptune Multi-Collector MC (ICP-MS) connected with a 193nm ArF (Geolas plus). The detailed analytical procedures for Hf isotope analysis can be found in Wu et al. (2006). Analytical spots were located in correspondence of different CL features and microstructures already characterized for U–Pb data and trace element. Analyses were carried out using a spot size of 65 μm with a frequency of 6Hz. Zircon GJ-1 and Mud Tank were taken as monitor

samples during analyses, and they gave weighted average $^{176}\text{Hf}/^{177}\text{Hf}$ values of 0.282011 ± 0.000022 (MSWD = 4.0, $n=10$) and 0.282515 ± 0.000008 (MSWD = 0.84, $n=12$), respectively. The obtained Hf isotopes are consistent with the recommended values for GJ-1 ($^{176}\text{Hf}/^{177}\text{Hf} = 0.282015 \pm 0.000019$; Elhlou et al., 2006) and Mud Tank (0.282507 ± 0.000006 ; Woodhead and Hergt, 2005). For more analytical detail see Appendix C, results are reported in Table A3.

4. Macroscopic structural features, petrography & mineral chemistry

A dyke swarm was recognized along the abandoned state road connecting the Finero village with the other villages of the valley (i.e., Orasso, Cursolo and Cannobio). We focused on three different dykes intruding mafic rocks of the External Gabbro unit (Fig. 1B). The dykes show sharp contacts with respect to the host rocks and have variable thickness up to 15 cm. Both the host rocks and the dykes show a well-developed mylonitic foliation and are affected by late faults (Fig. 2A, B, C). The dykes are randomly oriented with respect to the host rocks that show a mean attitude plunging at high angle toward N-NW (N330-340; Fig. 2D). One dyke has the same EW trend as reported by Stähle et al. (1990) for an alkaline dyke intruding the Mantle Peridotite unit a few hundred meters towards the NE (Fig. 1A, B and Fig. 2D).

The dykes consist of two distinct types of domain: i) plagioclase-rich (oligoclase; $\text{An}_{18-24}\text{Ab}_{79-82}\text{Or}_{0.3-0.7}$) domains, hereafter the leucocratic layers, and ii) thin layers and/or lenses of biotite and oxides, hereafter the melanocratic layers (Fig. 2E). Representative mineral analyses are reported in Table 2. Zircon, corundum and epidote are common accessory phases; apatite is rare and chlorite occurs locally as alteration products of biotite. A mylonitic fabric with well-developed porphyroclastic texture strongly overprints magmatic textures (Fig. 2E). Plagioclase porphyroclasts show deformation bands, undulose extinction, lobate contours; fractures and microscopic shear bands are also

common. The fine-grained matrix defines high-strain zones that are localized around porphyroclasts and is mainly made of completely recrystallized plagioclase (Fig. 3A), biotite and oxides. Locally, epidote and biotite define elongated aggregates (Fig. 3B). Biotite occurs along the mylonitic planes, it can be folded and may show kink of the cleavages, undulose extinction and deformation bands (Fig. 3B). Rarely, biotite is included within plagioclase porphyroclasts. Along the mylonitic planes, rounded grains of corundum is observed with up to 3 cm in length and 2 cm wide and is generally highly fractured and shows lobate contours (Fig. 3C, D). Euhedral grains of corundum are also common and enclosed within oxides (Fig. 3D). BSE-SEM images and chemical analyses revealed the occurrence of fine-grained interstitial K-feldspar within the matrix close to melanocratic layers (Table 2, Fig. 3D). Two main different oxides are present: magnetite is dominant, whereas Al-spinel is less common (Table 2; Fig. 3D). Along the completely recrystallized matrix a small grain of monazite was detected. This monazite grain is nearly homogeneous in BSE images with a small brighter area (Fig. 4A, B) compositionally different from the rest of the grain. The brighter area is characterized by a higher Th content (Table 2). The studied dykes can be classified as a quartz-free, zircon-and corundum-bearing diorite based on their mineral assemblages. At the hand-specimen scale, the composition of the dioritic dykes varies considerably, in some places being entirely feldspathic with narrow melanocratic layers, and elsewhere consisting of large corundum grains surrounded by plagioclase (Fig. 3E). In the latter case, the rock can be classified as plumasite (e.g. Gordon, 1922 and references therein), already reported as late intrusions within the mafic rocks and granulites (Kinzigite Formation) from the central and southern sectors of the IVZ (e.g. Rossi, 1968 and references therein).

The host rocks of the studied dykes consist of a metagabbro/diorite with a well-developed mylonitic fabric (Fig. A1.A): porphyroclasts comprise brown amphibole, pale-green clinopyroxene and plagioclase, whereas the fine-grained matrix consists of

recrystallized plagioclase (Plg-2) and amphibole (Amph-2; Fig. A1.B, C). Oxides are common, and titanite and zircon occur as accessories. Ultramafic lenses made of orthopyroxene, clinopyroxene, amphibole and oxides are observed (Fig. A1.A, D).

5. Zircon features

5.1. Zircon CL features

According to petrographic and textural characteristics, shapes and internal features zircon grains can be subdivided in two populations: i) zircon from the leucocratic layer and ii) zircon from the melanocratic layers.

In the leucocratic layers, zircon grains are large (up to 2 mm) and commonly occur as single grains and/or aggregates surrounded by a fine grained matrix consisting mainly of plagioclase. They have euhedral to subhedral shapes, with rare lobate grain boundaries (Fig. 4C-F). Embayments filled by biotite, spinel and plagioclase are also common (Fig. 4C-D). On CL images, zircon grains are either nearly homogeneous (Fig. 5A), or are sector zoned (e.g. Fig. 5B, C).

In the melanocratic layers, zircon grains/fragments are completely or partially surrounded by spinels \pm biotite, they commonly have rounded forms and lobate boundaries (Fig. 4F, Fig. 5D, E), and can contain inclusions of plagioclase, biotite and spinel. Internal zoning is complex: oscillatory, sector, broad-band and convoluted zoning may coexist within the same grain (Fig 5D, E, Fig. 6A-C). Commonly, the oscillatory and sector zoning may be unrelated with the crystal shapes or crystallographic orientation (Fig 5D, E, Fig. 6A-C). Locally, zoning features may show a continuity from different fragments (Fig. 6B). Moreover, small rounded zircon grains/fragments can be observed within the matrix, in the neighbouring region of larger grains (Fig. 6B).

In both textural contexts, zircon may show external domains darker with respect to the surrounding domains and with sharp irregular contacts.

5.2. Zircon brittle/ductile microstructures

Zircon grains contain numerous fractures with and without crystal displacement that define dense networks. These fractures may crosscut entire grains, connecting the innermost part with the matrix (Fig. 4C-F, Fig. 5A-E). Generally, different sets of approximately parallel fractures can be recognized. Commonly, one of these sets (generally the main set) is parallel or at low-angle with respect to the mylonitic foliation (Fig. 4D, Fig. 5E, Fig. 6A). Fractures delimit variably-sized polygonal domains defining a mosaic-like texture in CL images (Fig. 5A-E; Fig. 6A-C). Locally, network of narrow veins and black dots/areas under CL crosscut the zircon grain/fragment (Fig. 5D; Fig. 6A-C). The chemical composition (major and trace element) of the material filling the veins and of the black dots/areas has not been determined.

Zircon grains/fragments show clear evidence for both plastic and/or brittle deformation (Fig. 7 and Fig. 8). The most evident feature revealed by EBSD maps is the profuse occurrence of domains with uniform internal orientation but differing by ca. 5° (and occasionally by up to 10°) from the average orientation of the whole crystal. These features give the appearance of a mosaic texture of the crystal. These domain boundaries nicely coincide with brittle fractures revealed in BSE and CL images (Fig. 7 and 8) and therefore do not required intracrystal-plasticity to explain their occurrence (but see discussion below related to the feature shown in Fig. 8B). The biggest domains (ca. 100 μm) seem to form polygonal shapes with sharp boundaries. These are oriented following a particular direction (most probably corresponding to cleavage or parting along $\{100\}$ and occasionally $\{110\}$ planes, e.g. Fig. 8). Conversely, smaller domains ($< 100 \mu\text{m}$) do not follow any particular geometric arrangement nor a distinct gradient pattern in size (Fig. 6B and C).

One zircon fragment of Zrc1 from ALB-1B_mp (Zrc1) also shows evidence for a gradual change in orientation of up to ca. 20° over 100 μm (Fig. 8B, C) at one edge of the fragment

in contact with magnetite and other zircon fragments (Fig. 6 and Fig. 7). The area with gradual disorientation (Fig. 8B, C) has a slightly curve boundary towards the core of the crystal. The disorientation gradient is approximately constant and in the order of $0.25^{\circ}/\mu\text{m}$. Similar features have been described in detail by Reddy et al. (2007, their figure 5). In particular, this investigated domain is delimited and crosscut by sharp disorientations of 0.5° and 1° (Fig. 8B, C and supplementary figure A.2), which are interpreted to be related to brittle deformation.

An analysis of the rotation axis orientation (disorientations of $0.5-1^{\circ}$ and $1-2^{\circ}$) reveals that rotation axes are not randomly distributed in domains affected by brittle and ductile deformation. However, the crystallographic axis controlling the disorientation is different in both domains (Fig. 8E). Mosaic texture shows a single disorientation axis parallel to $[001]$ (Fig. 8E), whereas in the ductile domain rotation axes parallel to four symmetrically equivalent directions are observed, probably corresponding to poles to $\{201\}$ and $\{101\}$ (Fig. 8E). This later observation differs from the $[100]$ rotation axes most commonly found by Reddy et al. (2007).

High resolution EBSD mapping (with a step size of $1.5\ \mu\text{m}$, such as the one shown in Fig. 7 and others performed at $1\ \mu\text{m}$ steps in sample ALB-1A_mp, Fig. 8) enables to estimate the size distribution of the micro-domains separated by disorientation of 0.5° in the mosaic texture. An analysis of the size distribution of the mosaic domains in maps with a resolution of $1\ \mu\text{m}$ results in an average equivalent diameter of $5 \pm 8\ \mu\text{m}$ (defined as $2 \cdot \sqrt{(\text{area}/\pi)}$, where area is the measured grain section area).

5.3. LA-ICP-MS U–Pb analyses

5.3.1. U–Pb data of zircon from leucocratic layers

In both zircon grains from the ALB-1A sample, U–Pb data resulted mainly discordant with the exception of six ages from the Zrc2 (Fig. 9A-D).

Eighty-four laser spots were made on grain Zrc4, the $^{206}\text{Pb}/^{238}\text{U}$ ages show a large time span from 297 ± 12 to 219 ± 8 Ma and define two main clusters at approximately 260 and 240 Ma (Fig. 9A). The contour map of the $^{206}\text{Pb}/^{238}\text{U}$ dates shows that the younger dates (<240 Ma) define a main band/zone that broadly corresponds with darkest CL domains and is oriented parallel to fractures and the mylonitic foliation (whitish transparent area in Fig. 9B).

Forty-three U–Pb analyses were collected for the Zrc2 grain which is oriented oblique with respect to the mylonitic foliation (Fig. 5B). Data resulted mainly discordant with $^{206}\text{Pb}/^{238}\text{U}$ dates ranging from 296 ± 16 to 212 ± 10 Ma. Only 6 U–Pb ages are concordant and between 257 ± 14 Ma and 227 ± 10 Ma (Fig. 9C, D). Also in this case, the U–Pb data show a skewed distribution: the younger data ($^{206}\text{Pb}/^{238}\text{U} < 240$ Ma) were obtained from two opposite external sectors of the zircon grain located where foliation planes end against the grain margins at high angle, i.e. close to the pressure shadows (Fig. 9D); conversely, the oldest data were obtained from the other opposite sectors where foliation planes wrap around the grain (Fig. 9D).

5.3.2. U–Pb data of zircon from melanocratic layers

Sixteen and twenty-four analyses were collected in zircon grains (Zrc2 and Zrc3) almost completely surrounded by spinel and biotite grains from the ALB-1A_mp thin section (Fig. 5D, E). U–Pb data resulted mainly discordant and the $^{206}\text{Pb}/^{238}\text{U}$ dates range from 239 ± 8 to 221 ± 6 Ma and from 249 ± 8 to 210 ± 6 Ma for Zrc2 and Zrc3, respectively (Fig. 10A-D). No systematic distribution of the $^{206}\text{Pb}/^{238}\text{U}$ ages with respect to the zoning and position were observed for the two zircon grains (Zrc2 and Zrc3) from the ALB-1A_mp thin section. Nevertheless, only for Zrc2 we noted that the youngest $^{206}\text{Pb}/^{238}\text{U}$ age at about 220 Ma

was obtained from the external rim that shows alteration/recrystallization textures (Fig. 10A, B).

Fifty-four U–Pb data points were collected for different fragments of the Zrc1 grain within the ALB-1B_mp thin section (Fig. 6, 8, 10E-F). The data are mainly discordant (only 10 concordant analyses) and the $^{206}\text{Pb}/^{238}\text{U}$ ages vary from 248 ± 8 to 199 ± 6 Ma (Fig. 10E). The $^{206}\text{Pb}/^{238}\text{U}$ dates of Zrc1 grain show a broad preferential distribution: the youngest data derived from adjacent zircon domains that were previously intact and have been fragmented by fracturing, whereas the oldest data were obtained from the external domains, far from the fragmentation centre (Fig. 6, 8, 10E-F).

5.3.3. U–Th–Pb data of syn-kinematic monazite

Only three laser spots were collected from the small and elongated monazite grain found within the recrystallized matrix due to its small size. Two U–Th–Pb analyses were concordant at 180 ± 5 and 193 ± 6 Ma (Table A.2), the younger age was obtained from the darker BSE domain, which has lower concentration of Th relative to the bright domains. (Fig. 4B).

5.4. Trace element composition and Hf isotopes

5.4.1. Trace element composition of zircon from leucocratic layers

According to trace element distribution within the Zrc4 grain, two different domains can be recognized broadly corresponding to different CL features and $^{206}\text{Pb}/^{238}\text{U}$ data. The darker CL domains are characterized by higher (up to six times) concentrations of Nb, Ce, Ta, Pb, Th, U and HREE contents with respect to surrounding areas (Fig. 11 A-E). Even though the maximum concentrations of Nb, Ce, Ta, Pb, Th and U do not coincide with the highest values of the Y and HREE (Fig. 11B, C), these elements define concentric distributions with maxima aligned coherently with respect to the main internal fractures and

the mylonitic foliation that broadly correspond with the $^{206}\text{Pb}/^{238}\text{U}$ young band/zone (Fig. 4D, 5C, 9A, B and 11A). The Th/U ratio of Zrc4 is generally higher than 0.7 and in the central band an increase in Th over U is observed ($0.85 < \text{Th}/\text{U} < 1.42$, Fig. 11E). The U and Th contents of the central band are up to 200 and 274 ppm, respectively, whereas Y varies from 306 to 1223 ppm. The concentration of Hf does not change significantly from different areas and ranges from about 5400 to 7400 (Fig. 11F). The U/Yb ratio shows a difference between the two main areas being generally higher for the central darker CL band (Fig. 11F). The chondrite normalized REE patterns is characterized by a strong fractionation of HREE over LREE, a positive Ce anomaly and a weak or absent Eu anomaly. No significant difference between bright and dark domains was observed (Fig. 13A).

The trace element profiles performed on the Zrc2 grain do not reveal significant variations between the two selected orientations: i.e. parallel and at high-angle with respect to the mylonitic foliation (Fig. 11F). Trace element concentrations are generally comparable to those observed for Zrc4 from the same sample (Fig. 11D, E). In Zrc2 grain, the Hf content along the profile parallel to the mylonitic foliation is higher than the Hf content from the profile at high angle with respect to the foliation (Fig. 11E). Moreover, the spots from the darker CL domains are characterized by slightly lower Nb/Ta ratios ($4.5 < \text{Nb}/\text{Ta} < 5.4$) than the brighter domains ($6.7 < \text{Nb}/\text{Ta} < 8.9$). The chondrite normalized REE patterns (Fig. 13B) of the two profiles are similar and characterized by a strong fractionation of HREE over LREE, a positive Ce anomaly and a weak or absent Eu anomaly.

5.4.2. Trace element composition and Hf isotopes of zircon from melanocratic layers

The trace element composition and Hf isotopes of zircon grains/fragments from the melanocratic layers were determined in order to characterize the elemental and isotopic

composition of the different zoning patterns and microstructures. Some data are shown in Fig. 12A, B, C, the location of the analytical spots is shown in Fig. 10B, D and F.

The lowest Th/U ratios and the highest Hf contents (up to 9453 ppm) were obtained from the external rims characterized by broad banding zoning. One rim analysis yields also the highest U/Yb ratio (up to 1.6, ALB1A_mp; 11_Zrc2_i). The domains with the oscillatory zoning provided the highest Th/U ratios (up to 2.0). In the fragments of Zrc1 from ALB-1B_mp sample, these domains show the youngest $^{206}\text{Pb}/^{238}\text{U}$ data (Fig. 10C, D). The ϵHf values are positive and range from +0.2 to +4 (Fig. 12C) without clear relationships with internal zoning or position within the grain/fragment. The ϵHf values are lower than those reported by Schaltegger et al. (2015) for the megacrystic zircon in nepheline diorite pegmatites ($6.4 < \epsilon\text{Hf} < 9.8$) from the northeastern sector of the Finero Mafic complex (see Fig. 1A), but significantly higher than those determined in chromitite zircons from the mantle Phlogopite Peridotite unit ($-6 < \epsilon\text{Hf} < -2$; Zanetti et al., 2016 and references therein). Also for those grains/fragments, the chondrite normalized REE patterns are characterized by a strong dominance of HREE over LREE, a common positive Ce anomaly and a weak or absent Eu anomaly (Fig. 13C-E).

6. Discussion

6.1. Zircon chemistry and microstructures

In the leucocratic layers, the large (up to 2 mm) zircon grains show euhedral (magmatic) shapes and primary CL features, such as sector zoning (i.e. Zrc2 from ALB-1A, Fig. 5) indicating growth under magmatic conditions (e.g. Hanchar & Miller, 1993; Corfu et al., 2003). These grains do not show evidence of crystal-plastic deformation, they are crosscut by numerous fractures connecting their innermost portion with the matrix and potentially allowing chemical and isotopic modification due to mass transfer and diffusive exchange. Zircon grains from the leucocratic layers provided the oldest $^{206}\text{Pb}/^{238}\text{U}$ dates

suggesting a minimum crystallization age during Late Carboniferous. The age mapping of the grain also reveals the occurrence of significantly younger ages (<240Ma) which are preferentially distributed parallel to the main fracture set and the foliation planes or adjacent to pressure shadows (Fig. 9A-D). These youngest domains are also characterised by REE-enrichment and higher Th/U ratios with respect to the surrounding domains. A similar relationship between age, trace element composition and microstructure was previously observed by Moser et al. (2009), Nemchin et al. (2009), Piazzolo et al. (2012) and Grange et al. (2013) and reinforce the evidence that post crystallisation history of zircon, even in absence of clear recrystallization, may affect geochronological results.

Except for comparable dimensions, zircon grains from melanocratic layers are characterized by different shapes and internal features and yield only Late Permian to Early Jurassic $^{206}\text{Pb}/^{238}\text{U}$ ages. They can contain domains with internal zoning features discordant with the surrounding sectors and/or unrelated with the crystal shapes or crystallographic orientation (Fig. 5 and 6). CL images further revealed that the zircon aggregates may represent fragments separated and displaced from a large pre-existing single grain (e.g. Fig. 6A). These aggregates formed mainly by fragmentation and subsequent rotation and displacement in the fine-grained matrix (e.g. Piazzolo et al., 2012). The fragments can be restored, back rotating and translating, to their original position with almost perfect match of the grain boundaries, with the exception of new small grains and overgrowths. According to EBSD mapping, intracrystalline deformation is rare and mainly localized at the edges of the fragments previously in contact (former zircon-zircon boundary). These edges show distortion with bending and relative misorientation up to 20° , have a radial semi-circular shape with a sharp boundary with undeformed domain (i.e., type 2 distortion of Piazzolo et al., 2012). They can be also characterized by a less misorientation degree and a gradual transition towards undeformed domains (e.g., type 1

distortion of Piazzolo et al., 2012). The lattice distortion patterns observed for the Zrc1 from the melanocratic layer is comparable to that observed in zircon from mylonites associated with pseudotachylites (Kovaleva et al., 2015) and without pseudotachylites (e.g. Reddy et al., 2007; Piazzolo et al., 2012; Kovaleva et al., 2014).

6.2. *The multi-stage evolution recorded by zircon*

Two alternative hypotheses can be proposed for the dyke crystallization and subsequent evolution based on the systematic differences observed between zircon from leucocratic and melanocratic layers: i) dyke crystallized during Late Permian to early Jurassic, or ii) it experienced a multistage evolution with Late Carboniferous-Early Permian crystallization and later crystallization/recrystallization events.

In the first hypothesis, the zircon grains from the leucocratic layers showing old ages up to Late Carboniferous should be considered as xenocrystic grains scavenged from the surrounding mafic/ultramafic and basement rocks. Consequently, the old ages indicate inheritance. However, the euhedral shapes and primary CL feature of these zircon grains let us to prefer the second hypothesis. In this scenario, zircon grains from the leucocratic layers can be considered as crystallized directly from the melt and experienced subsequent microstructural, isotopic and chemical modifications. Some constrains on the chemistry of the later event can be proposed on the basis of the trace element variations in zircon. The relative enrichment of some trace elements with respect to the others (i.e. Zrc4 from the leucocratic layer) may suggest a possible net influx into the grains from an external source. According to Timms et al. (2006), a chemical gradient between the zircon grains and a source highly enriched in incompatible elements, such as U, Th and Pb, could provide a driving force for the observed trace element diffusion into zircon. The substantial increase in Th/U ratio along the bands/zone parallel to the mylonitic foliation

(i.e. Zrc4 and Zrc2) reflects element partitioning between zircon grains and the source, solid or fluid, during deformation and/or annealing of the grains.

The origin of zircon grains from the melanocratic layers remains still cryptic. Two alternative hypotheses can be proposed: i) they represent inherited grains from the leucocratic layers or some other source (e.g. scavenged from surrounding host rocks); ii) they represent newly formed grains. The rounded and anhedral shapes, the complex CL features and the $^{206}\text{Pb}/^{238}\text{U}$ ages indicate that zircon grains from the melanocratic layers can be considered as composite grains consisting of both inherited and newly formed domains. This hypothesis can explain the occurrence of oscillatory zoned inner domains truncated by zircon domains with different CL properties. It can also be applied in order to explain the occurrence of fragments derived from the fragmentation of pre-existing larger grains. In this scenario, the origin of these composite grains can be linked to the formation of the melanocratic layers. The age of formation of the melanocratic layers is difficult to constrain. However, the most common oldest ages in these zircon grains are close to 250 Ma, and likely represent the age of the metasomatic event that overprinted the dyke system after emplacement with crystallization/recrystallization of zircon. It is worth to note that late intrusive and/or metasomatic events providing Late Triassic to Early Jurassic ages have been described within the mafic/ultramafic rocks lying structurally below the studied lithological unit (Stähle et al., 1990, 2001; Grieco et al., 2001; Matsumoto et al., 2005; Morishita et al., 2008, Schaltegger et al., 2015).

In both textural sites, zircon grains show an irregular rim with a variable thickness characterized by planar and/or broad-band CL zoning (Fig. 5, 6 and 7). The boundary between the rim and the inner portion is curved and sharp, more akin to a chemical reaction front than a diffusion interface, suggesting a later replacement/recrystallization process (e.g. Schaltegger et al., 1999) propagating inward the zircon grain. Generally, these rims are too small to be analysed (dating and trace elements) with LA-ICP-MS. Only in a few cases it was possible to determine both the ages and the trace element composition and we obtained the

lowest Th/U ratio (<0.5) and a Late Triassic $^{206}\text{Pb}/^{238}\text{U}$ date at 210 ± 6 Ma (e.g. Fig. 10D; spot “u”). Interestingly, the U–Pb dating of a single monazite grain within the foliation yielded Early Jurassic concordant ages, which are only slightly younger than the ages of some external zircon rims. These younger dates are tentatively interpreted as the age of the regional-scale thermal event (e.g. Zanetti et al., 2016 and references therein) and associated mylonitic deformation that have been documented also within gabbros/diorites hosting the dyke swarm (e.g. Langone et al., 2016, Degli Alessandrini et al., 2016). This thermal event is also responsible of the spread in dates towards younger ages found in zircon of both the leucocratic and melanocratic domains.

By combining microstructural observations of the zircon grains and their trace element and isotope geochemistry, we tentatively suggest a multi-stage evolution of the studied dykes synthesized in Figure 14. Zircon grains record a complex multi-stage evolution consisting in the following major steps: i) a minimum age of emplacement of the dyke at 297 Ma (Fig. 14A); ii) a tectonic-magmatic event inducing deformation coeval with pervasive migration of exotic fluids/melts (melanocratic layer) during the Late Permian (Fig. 14B); iii) partial resetting of the U–Pb system during Late Triassic – Early Jurassic in response to a regional-scale thermal event which promoted a localized recrystallization process that was characterized by a lower fluid/zircon ratio and occurred coevally with the formation of other U, Th and REE bearing phases, such as monazite and titanite (Fig. 14C).

6.3. Regional implications

Our microstructural observations, isotopic and geochemical data have important implications for the evolution of the northeastern sector of the Ivrea-Verbano Zone.

Plagioclase-rich pegmatites and dykes with alkaline affinity are reported as intrusion within the mafic/ultramafic rocks of the northeastern sector of the IVZ (Fig. 1A, B), from the

Italian village of Finero to the Val Boschetto in Switzerland (i.e. Stähle et al., 1990; 2001; Oppizzi & Schaltegger, 1999; Grieco et al., 2001; Schaltegger et al., 2015). The U-Pb dating of zircon from these late magmatic products indicate multiple intrusions from Late Triassic to Early Jurassic (Fig. 15). According to Schaltegger et al. (2015) the alkaline melts intruded at lower crustal levels between 212.5 and 190 Ma in different pulses. Slightly older zircon ages were obtained by Stähle et al. (1990) from 7 zircon fragments from a syenite pegmatite close to the Finero village (Fig. 1, 15). These authors reported uncorrected $^{207}\text{Pb}/^{206}\text{Pb}$ data ranging from 233 ± 28 Ma to 222 ± 10 Ma and a common-Pb corrected $^{207}\text{Pb}/^{206}\text{Pb}$ age of 225 ± 13 Ma that they interpreted as the emplacement age of the dyke. The results of Stähle et al. (1990) enlarge the time span of the alkaline magmatism and partially overlap, within errors, the intrusion ages provided for the other alkaline dykes/pegmatites (Oppizzi & Schaltegger, 1999; Grieco et al., 2001; Schaltegger et al., 2015) and is in agreement with the intrusion and post-crystallization history of the External Gabbro unit (i.e. Zanetti et al. 2013; SHRIMP U-Pb zircon dating; Fig. 15). These observations suggest a possible scenario where large volume of mafic magma intruded at the base of the lower crust (i.e. External Gabbro unit, Zanetti et al., 2013) coevally (within the uncertainty of the data) and/or slightly predating multiple injections of alkaline dykes and pegmatites intruded within the lowermost structural units (i.e., Mantle Peridotite unit, L.I.Z. and Amphibole Peridotite unit; Stähle et al., 1990 Oppizzi & Schaltegger, 1999; Grieco et al., 2001; Schaltegger et al., 2015; Fig. 1 and 15). Here we report the first occurrence of zircon- and corundum-bearing dioritic dykes within the uppermost unit, i.e. the External Gabbro (Fig. 1A, B, Fig. 15). Studied dykes share numerous affinities with the pegmatites and dykes reported by other authors, i.e. mineral assemblages, macrostructures and brittle/ductile deformation features. However, they are significantly different in terms of emplacement age, evolution and geochemical affinity. The studied dykes intruded largely earlier (Late Carboniferous – Early Permian?) and experienced a

subsequent metasomatic event (Late Permian - Early Triassic). Besides, Hf isotopic zircon composition is different with respect that documented by Schaltegger et al. (2015) in both foid-free and nepheline-bearing diorite pegmatites. Thus, the interpretation of zircon ages obtained in this work may have important implications for the regional geology. Zircon grains from both leucocratic and melanocratic layers provided U–Pb ages older than the emplacement age of the host rocks, i.e. the mafic rocks of the External Gabbro unit intruded in Middle Triassic time (Zanetti et al., 2013). By interpreting the zircon grains as inherited from the surrounding magmatic and metamorphic rocks our results would be irrelevant for the magmatic evolution of the whole unit (Fig. 15). Conversely, a primary magmatic origin for the studied zircon grains would have important repercussions for the tectono-metamorphic and magmatic evolution of the northeastern sector of the IVZ. As discussed above, studied zircon grains indicate a multi-stage evolution with crystallization from a melt, during Late Carboniferous - Early Permian, and a subsequent metasomatic overprint, occurred probably during Late Permian. This imply that the mafic rocks hosting the dated dykes also intruded before the Triassic (Fig. 15). Therefore, the External Gabbro unit, considered until now a Middle Triassic magmatic body (i.e. Zanetti et al., 2013), should be considered as a composite mafic complex with multiple intrusions from Late Carboniferous - Early Permian, as in the central and southern sectors of the IVZ (e.g. Peressini et al., 2007, Klötzli et al., 2014), to Middle Triassic (e.g. Zanetti et al., 2013).

Our results imply also that multiple injections of dioritic dykes and pegmatites occurred in a large time span, from Permian to Jurassic, at lower crustal levels suggesting a long persistence of high-temperature conditions. This is coherent with recent interpretations of U-Pb zircon dating from chromitite layers within the Mantle Peridotite unit of the Finero Mafic Complex (e.g., Grieco et al., 2001; Badanina & Malitch, 2012; Badanina et al., 2013 and Zanetti et al., 2016; Fig. 15). According to Badanina & Malitch (2012) and Badanina et al. (2013) the U-Pb ages from Permian to Jurassic suggest a

prolonged formation and multistage evolution of zircon growth within the mantle body. Alternatively, Zanetti et al. (2016) proposed that the chromitite layers intruded before (late Permian) and experienced prolonged resetting of the U-Pb system ending with an important reheating event during early Jurassic time (Fig. 15). The maintenance of high temperature conditions at lower crustal levels from Late Carboniferous to Early Permian has recently been also suggested for the central IVZ (i.e. Klötzli et al., 2014).

7. Conclusions

- The coupling of morphological and CL features of zircon grains with information about their textural location, U–Pb geochronology and trace element geochemistry allowed us to track the multi-stage evolution of the dyke-system composed of distinct layers: i.e. leucocratic and melanocratic. We showed that zircon internal features (CL zoning, CPO, fractures, cracks), chemistry and $^{206}\text{Pb}/^{238}\text{U}$ dates distribution are strongly linked to the mylonitic fabric and textural position.
- Zircon grains from the leucocratic layers are euhedral to subhedral and show primary magmatic features homogeneously distributed all over the grain. Zircon grains from the melanocratic layers have rounded shapes and are characterised by more complex CL features commonly without any relationship with the crystal shapes or crystallographic orientation.
- Zircon grains show evidence for both brittle and intracrystalline deformation. Fractures are common and well visible. Generally, they are parallel with respect to the mylonitic foliation. Intracrystalline deformation is mainly due to fragmentation of a former larger grain: a gradual change in orientation of up to ca. 20° over 100 μm was observed at the edges of fragments that were previously in contact (zircon-zircon boundary).
- U–Pb data of zircon resulted mainly discordant. Zircon grains from the leucocratic layers show a larger variation of the $^{206}\text{Pb}/^{238}\text{U}$ ages, from Late Carboniferous to Early Jurassic,

with respect to zircon grains from the melanocratic layers, providing $^{206}\text{Pb}/^{238}\text{U}$ ages always younger than Late Permian. The within grain distribution of $^{206}\text{Pb}/^{238}\text{U}$ ages for zircon grains from the leucocratic layers revealed that the younger ages were obtained from inner bands/sectors oriented parallel to fractures and the mylonitic foliation or placed in contact with pressure shadows. The ages distribution broadly corresponds with the trace element variations: the younger domains are generally associated with enrichments of Nb, Ce, Ta, Pb, Th, U and HREE.

- The dykes experienced a multi-stage evolution consisting in a first crystallization of the leucocratic domains, during Late Carboniferous – Early Permian followed by annealing and reorganization of zircon grains during a (K-rich) metasomatic event produced by injection and crystallization of the melanocratic layers (biotite+oxides). This metasomatic overprint affected the whole dyke system but was more pronounced for those zircon grains that experienced a partial or total interaction with the metasomatic agent.
- Our study further suggests that for dating zircon in presence of deformation (i.e. zircon porphyroclasts) the use of microanalytical techniques directly on thin section is highly recommended.
- Results from the present study have important implications in the geology of the Ivrea-Verbano Zone because, having the dyke intruded the External Gabbro unit before Triassic (probably during Late Carboniferous – Early Permian), the latter cannot be considered a Triassic intrusion. At least part of the External Gabbro unit is older as the other mafic bodies of the Ivrea-Verbano Zone. Our results highlight the necessity of a more detailed petrographic, geochemical and geochronological characterization of mafic rocks of the External Gabbro unit which are affected by high temperature metamorphic overprint, metasomatism and brittle-ductile deformation.

Acknowledgements

This work was funded by the MIUR PRIN 2015 “Geochemical and isotopic budget of highly metasomatised sub-continental mantle in the Africa and Europe geodynamic systems: modern and fossil analogues”; and by a Short Term Mobility (2015; A. Langone) of the CNR (Italy). N.E. Timms and U.S. Klötzli are thanked for the constructive reviews of the manuscript.

REFERENCES

Badanina, I.Yu., Malitch, K.N., 2012. Timing of metasomatism in a subcontinental mantle: evidence from zircon at Finero (Italy). EGU general assembly, 14.

Badanina, I.Yu., Malitch, K.N., Belusova, E.A., 2013. U-Pb and Hf isotope characteristics of zircon from chromitites at Finero. Goldschmidt conference abstract.

Black, L.P., Gulson, B.L., 1978. The age of the Mud Tank carbonatite, Strangways Range, Northern Territory. BMR J. Aust. Geol. Geophys. 3, 227–232.

Blichert-Toft, J., Chauvel, C., Albarede, F., 1997. Separation of Hf and Lu for high-precision 750 isotope analysis of rock samples by magnetic sector-multiple collector ICP–MS. Contributions to Mineralogy and Petrology 127, 248–260.

Boriani, A., Burlini, L., Sacchi, R., 1990. The Cossato–Mergozzo–Brissago Line and the Pogallo Line (southern Alps, Northern Italy) and their relationships with the late–Hercynian magmatic and metamorphic events. Tectonophysics, 182, 91–102.

Cherniak, D.J., Watson E.B., 2003. Diffusion in zircon, in: Hanchar, J.M. Hoskin, P.W.O. (Eds), Zircon. Reviews in Mineralogy and Geochemistry, Mineralogical Society of America, pp 113-144.

Corfu, F., Hanchar, J.M., Hoskin, P.W.O., Kinny, P. (2003) Atlas of zircon textures, in: Hanchar, J.M. Hoskin, P.W.O. (Eds), Zircon. Reviews in Mineralogy and Geochemistry, Mineralogical Society of America, pp. 469–500.

Degli Alessandrini, G., Menegon, L., Beltrando, M., Gijksstra, A., Anderson, M., 2016. Metamorphic reactions, grain size reduction and deformation of mafic lower crustal rocks. Geophysical Research Abstracts 18, EGU2016-13587, 2016 EGU General Assembly 2016.

Elhlou, S., Belousova, E., Griffin, W.L., Pearson, N.J., O'reilly, S.Y., 2006. Trace element and isotopic composition of GJ red zircon standard by laser ablation. *Geochimica et Cosmochimica Acta* 70, A158 (Supplement 1).

Ewing, T.A., Rubatto, D., Beltrando M., Hermann J., 2015. Constraints on the thermal evolution of the Adriatic margin during Jurassic continental break-up: U–Pb dating of rutile from the Ivrea-Verbano Zone, Italy. *Contributions to Mineralogy and Petrology*, 169, DOI 10.1007/s00410-015-1135-6.

French, J.E. and Heaman, L.M., 2010. Precise U-Pb dating of Paleoproterozoic mafic dyke 987 swarms of the Dharwar craton, India: Implications for the existence of the Neoproterozoic supercraton Sclavia. *Precambrian Research* 183, 416-441.

- Gasquet, D., Bertrand, J.M., Paquette, J.L., Lehmann, J., Ratzov, G., De Ascensão Guedes, R., Tiepolo, M., Boullier, A.M., Scaillet, S., Nomade, S., 2010. Miocene to Messinian deformation and hydrothermal activity in a pre-Alpine basement massif of the French western Alps: new U–Th–Pb and argon ages from the Lauzière massif. *Bulletin de la Société Géologique de France*, 181, 227-241.
- Geisler, T., Pidgeon, R.T., van Bronswijk, W., Pleyzier, R., 2001. Kinetics of thermal recovery and recrystallization of partially metamict zircon: a Raman spectroscopic study. *European Journal of Mineralogy* 13, 1163–1176.
- Gordon, S.G., 1922. The mineralogy of Pennsylvania. Academy of Natural Sciences, Philadelphia, Special Publication, 1, 260 pp.
- Grieco, G., Ferrario, A., von Quadt, A., Köppel, V., Mathez, A., 2001. The zircon-bearing chromitites of the phlogopite peridotite of Finero (Ivrea Zone, Southern Alps): evidence and geochronology of a metasomatized mantle slab. *Journal of Petrology* 42, 89–101.
- Hanchar, J.M., Miller, C.F., 1993. Zircon zonation patterns as revealed by cathodoluminescence and backscattered electron images: implications for interpretation of complex crustal histories. *Chemical Geology* 110, 1–13.
- Harley, S.L., Kelly, N.M., 2007. Zircon tiny but timely. *Elements* 3, 13–18.
- Hazen, R. M., Finger, L. W., 1979. Crystal structure and compressibility of zircon at high pressure. *American Mineralogist* 64, 196-201.

- Hiess, J., Condon, D.J., McLean, N., Noble, S.R., 2012. $^{238}\text{U}/^{235}\text{U}$ systematics in terrestrial Uranium-bearing minerals. *Geology* 335, 1610–1614.
- Hingerl, F., Klötzli, U., Steuber, C., Kleinschrodt, R., 2008. New results from the mafic complex in the Finero area. 33th International Geological Congress, Oslo 6–14 August 2008, CDROM abstracts, X-CD Technologies. Available at <http://www.cprm.gov.br/33IGC/1344964.html>.
- Horstwood, M.S.A., Foster, G.L., Parrish, R.R., Noble, S.R., Nowell, G.M., 2003. Common-Pb corrected in situ U–Pb accessory mineral geochronology by LA–MC–ICP–MS. *Journal of Analytical Atomic Spectrometry* 18, 837–846.
- Iizuka, T., Hirata, T., 2005. Improvements of precision and accuracy in in-situ Hf isotope microanalysis of zircon using the laser ablation-MC-ICPMS technique. *Chemical Geology* 220, 121–137.
- Jackson, S.E., Pearson, N.J., Griffin, W.L., Belousova, E., 2004. The application of laser ablation inductively coupled plasma mass spectrometry to in situ U–Pb zircon geochronology. *Chemical Geology* 211, 47–69.
- Kaczmarek, M.-A., Reddy, S.M., Timms, N.E., 2011. Evolution of deformation mechanism in a shear zone (Lanzo massif, Western-Alps). *Lithos* 127, 414–426.
- Kenkmann, T., 2000. Processes controlling the shrinkage of porphyroclasts in gabbroic shear zones. *Journal of Structural Geology* 22, 471–487.

Klötzli, U., Hochleitner, R., Kosler, J., 2007. Lower Triassic mantle-derived magmatism in the Ivrea-Verbano Zone: evidence from laser ablation U-Pb dating of a pegmatite from the eastern Finero Complex (Switzerland). *Mitteilungen der Österreichischen Mineralogischen Gesellschaft* 153, 65.

Klötzli, U., Klötzli, E., Günes, Z., Kosler, J., 2009. Accuracy of laser ablation U-Pb zircon dating: results from a test using five different reference zircons. *Geostandards and Geoanalytical Research* 33(1), 5-15.

Klötzli, U., Sinigoi, S., Quick, J.M., Demarchi, G., Tassinari, C.C.G., Sato, K., Günes, Z., 2014. Duration of igneous activity in the Sesia Magmatic System and implications for high-temperature metamorphism in the Ivrea-Verbano deep crust. *Lithos* 206–207, 19–33,

Kovaleva, E., Klötzli, U., Habler, G., Libowitzky E., 2014. Finite lattice distortion patterns in plastically deformed zircon grains. *Solid Earth*, 5, 1099-1122.

Kovaleva, E., Klötzli, U., Habler, G., Wheeler, J., 2015. Planar microstructures in zircon from paleo-seismic zones. *American Mineralogist*, 100, 1834–1847.

Kretz, R., 1983. Symbols for rock-forming minerals. *American Mineralogist* 68, 277-279.

Langone, A., Tiepolo, M., 2015. U-Th-Pb “multi-phase” approach to the study of crystalline basement: application to the northernmost sector of the Ivrea-Verbano Zone (Alps). *Periodico di Mineralogia*, 84, 633-655.

Langone, A., Zanetti, A., Tiepolo, M., Mazzucchelli, M., 2016. Dating the onset of a lower crustal shear zone: a (lucky) case from the northern sector of the Ivrea-Verbano Zone (Val Cannobina, Italy). European Mineralogical Conference, Abstract, 638.

Ludwig, K.R., 2003. Isoplot/Ex version 3.0: a geochronological toolkit for Microsoft Excel. Berkeley Geochronology Center Special Publication 4. Berkeley, Berkeley Geochronology Center, 70 p.

MacDonald, J.M., Wheeler, J., Harley, S.L., Mariani, E., Goodenough, K.M., Crowley, Q., Tatham, D., 2013. Lattice distortion in a zircon population and its effects on trace element mobility and U–Th–Pb isotope systematics: examples from the Lewisian Gneiss Complex, northwest Scotland. Contributions to Mineralogy and Petrology, 166, 21–41.

McDonough, W. F., Sun, S.S., 1995. The composition of the Earth. Chemical Geology 120, 23–253.

Mazzucchelli, M., Quick, J.E., Sinigoi, S., Zanetti, A., Giovanardi, T., 2014. Igneous evolutions across the Ivrea crustal section: the Permian Sesia magmatic system and the Triassic Finero intrusion and mantle. Goldschmidt conference – Florence, 2013. Geological Field Trips 6 (2.2), 98. <http://dx.doi.org/10.3301/GFT.2014.05> (ISSN: 2038-4947).

Matsumoto, T., Morishita, T., Masuda, J., Fujioka, T., Takebe, M., Yamamoto, K., Arai, S., 2005. Noble gases in the Finero Phlogopite-Peridotites, Italian Western Alps. Earth and Planetary Science Letters 238, 130-145.

Moser, D.E., Davis, W.J., Reddy, S.M., Flemming, R.L., Hart, R.J., 2009. Zircon U–Pb strain chronometry reveals deep impact-triggered flow. *Earth and Planetary Science Letters* 277, 73–79.

Morishita, T., Hattori, K. H., Terada, K., Matsumoto, T., Yamamoto, K., Takebe, M., Ishida, Y., Tamura, A., Arai, S., 2008. Geochemistry of apatite-rich layers in the Finero phlogopite-peridotite massif (Italian Western Alps) and ion microprobe dating of apatite. *Chemical Geology* 251, 99–111.

Nemchin, A., Timms, N., Pidgeon, R., Geisler, T., Reddy, S., Meyer, C., 2009. Timing of crystallization of the lunar magma ocean constrained by the oldest zircon. *Nat. Geosci.* 2(2), 133–136.

Oppizzi, P., Schaltegger, U., 1999. Zircon bearing plagioclases from the Finero complex (Ivrea zone): dating a Late Triassic mantle hic-cup? *Schweizerische Mineralogische und Petrographische Mitteilungen* 79, 330–331.

Pearce, N.J.G., Perkins, W.T., Westgate, J.A., Gorton, M.P., Jackson, S.E., Neal, C.R., Chenery, S.P., 1997. A compilation of new and published major and trace element data for NIST SRM 610 and NIST SRM 612 glass reference materials. *Geostandards Newsletter* 21, 115–144.

Peressini, G., Quick, J. E., Sinigoi, S., Hofmann, A.W., Fanning, M., 2007. Duration of a large mafic intrusion and heat transfer in the lower crust: a SHRIMP U/Pb zircon study in the Ivrea-Verbano Zone (Western Alps, Italy). *Journal of Petrology* 48, 1185–1218.

Peterman, E.M., Reddy, S.M., Saxey, D.W., Snoeyenbos, D.R., Rickard, W.D., Fougere, D., Kylander-Clark, A.R., 2016. Nanogeochronology of discordant zircon measured by atom probe microscopy of Pb-enriched dislocation loops. *Sci. Adv.* 2 (9), e1601318.

Piazolo, S., Austrheim, H., Whitehouse, M., 2012. Brittle-ductile microfabrics in naturally deformed zircon: Deformation mechanisms and consequences for U-Pb dating. *American Mineralogist*, 97, 1544–1563.

Piazolo, S., La Fontaine, A., Trimby, P., Harley, S., Yang, L., Armstrong, R., Cairney, J.M., 2016. Deformation-induced trace element redistribution in zircon revealed using atom probe tomography. *Nature Communications* 7:10490 (DOI: 10.1038/ncomms10490)

Quick, J. E., Sinigoi, S., Mayer, A., 1995. Emplacement of mantle peridotite in the lower continental crust, Ivrea-Verbano Zone, northwest Italy. *Geology* 23(8), 739-742.

Quick, J. E., Sinigoi, S., Peressini, G., Demarchi, G., Wooden, J., Sbisà, A., 2009. Magmatic plumbing of a large Permian caldera exposed to a depth of 25 kilometers. *Geology* 37(7), 603-606, doi:10.1130/G30003A.1.

Reddy, S.M., Timms, N.E., Trimby, P., Kinny, P.D., Buchan, C., Blake, K., 2006. Crystal-plastic deformation of zircon: a defect in the assumption of chemical robustness. *Geology*, 34, 257–260.

Reddy, S.M., Timms, N.E., Pantleon, W., Trimby, P., 2007. Quantitative characterization of plastic deformation of zircon and geological implications. *Contributions of Mineralogy and Petrology*, 625-645.

Reddy, S.M., van Riessen, A., Saxey, D.W., Johnson, T.E., Rickard, W.D., Fougereuse, D., Fischer, S., Prosa, T.J., Rice, K.P., Reinhard, D.A., Chen, Y., 2016. Mechanisms of deformation-induced trace element migration in zircon resolved by atom probe and correlative microscopy. *Geochim. Cosmochim. Acta* 195, 158–170.

Rimša, A., Whitehouse, M.J., Johansson, L., Piazzolo, S., 2007. Brittle fracturing and fracture healing of zircon: An integrated cathodoluminescence, EBSD, U-Th-Pb, and REE study. *American Mineralogist* 92, 1213-12-24.

Rossi, A., 1968. Le rocce corindonifere del “Croso della Gavala” (Valsesia-Vercelli). *Schweizerische mineralogische und petrographische Mitteilungen* 48, 67-74.

Schaltegger, U., Fanning, C. M., Günther, D., Maurin, J. C., Schulmann, K., Gebauer, D., 1999. Growth, annealing and recrystallization of zircon and preservation of monazite in high-grade metamorphism. Conventional and in-situ U-Pb isotope, cathodoluminescence and microchemical evidence. *Contributions to Mineralogy and Petrology* 134, 186-201.

Schaltegger, U., Ulianov, A., Muntener O., Ovtcharova M., Peytcheva, I., Vonlanthen P., Vennemann, T., Antognini, M., Girlanda, F., 2015. Megacrystic zircon with planar fractures in miaskite–type nepheline pegmatites formed at high pressures in the lower crust (Ivrea Zone, southern Alps, Switzerland). *American Mineralogist*, 100, 83–94.

- Schmid, S.M. 1993. Ivrea zone and adjacent southern Alpine basement. In: von Raumer, J.F., Neubauer, F. (Eds.), *Pre-Mesozoic Geology in the Alps*. Springer-Verlag, Berlin, pp. 567–583.
- Seydoux-Guillaume, A.M., Paquette, J.L., Wiedenbeck, M., Montel, J.M., Heinrich W., 2002a. Experimental resetting of the U–Th–Pb system in monazite. *Chemical Geology* 191, 165–181.
- Seydoux-Guillaume, A.M., Wirth, R., Nasdala, L., Gottschalk, M., Montel, J.M. Heinrich, W., 2002b. XRD, TEM and Raman study of experimental annealing of natural monazite. *Physics and Chemistry of Minerals* 29, 240–253.
- Siena, F., Coltorti, M., 1989. The petrogenesis of a hydrated mafic–ultramafic complex and the role of amphibole fractionation at Finero (Italian Western Alps). *Neues Jahrbuch für Mineralogie* 6, 255–274.
- Stähle, V., Frenzel, G., Kober, B., Michard, A., Puchelt, H., Schneider, W., 1990. Zircon syenite pegmatites in the Finero peridotite (Ivrea Zone): evidence for a syenite from a mantle source. *Earth and Planetary Science Letters* 101, 196–205.
- Stähle, V., Frenzel, G., Hess, J.C., Saupé, F., Schmidt, S.T., Schneider, W., 2001. Permian metabasalt and Triassic alkaline dykes in the northern Ivrea Zone: clues to the post-Variscan geodynamic evolution of the Southern Alps. *Schweizerische Mineralogische und Petrographische Mitteilungen* 81, 1–21.

Steck, A., Tièche, J. C., 1976. Carte géologique de l'antiforme péridotitique de Finero avec des observations sur les phases de déformation et de recristallisation. Bulletin Suisse de Minéralogie et de Pétrographie 56, 501-512.

Timms, N.E., Reddy, S.M., 2009. Response of cathodoluminescence to crystal-plastic deformation in zircon. Chem. Geol. 261 (1–2), 12–24.

Timms, N.E., Kinny, P., Reddy, S.M., 2006. Enhanced diffusion of uranium and thorium linked to crystal plasticity in zircon. Geochemical Transactions 7:10.

Timms, N.E., Kinny, P., Reddy, S.M., Evans, K., Clark, C., Healy, D., 2011. Relationship among titanium, rare earth elements, U–Pb ages and deformation microstructures in zircon: Implications for Ti-in-zircon thermometry. Chemical Geology, 280, 33-46.

Timms, N.E., Erickson, T.M., Pearce, M.A., Cavoise, A.J., Schmieder, M., Tohver, E., Reddy, S.M., Zanetti, M.R., Nemchin, A.A., Wittmann, A., 2017. A pressure-temperature diagram for zircon at extreme conditions. Earth-Sciences Reviews, 165, 185-202.

Tretiakova, I.G., Belousova, E.A., Malkovets, V.G., Griffin, W.L., Piazzolo, S., Pearson, N.J., O'Reilly, S., Nishido, H., 2017. Recurrent magmatic activity on a lithosphere-scale structure: crystallization and deformation in kimberlitic zircons. Gondwana Res., 126-132

Valley, J.W., Cavoise, A.J., Ushikubo, T., Reinhard, D.A., Lawrence, D.F., Larson, D.J., Clifton, P.H., Kelly, T.F., Wilde, S.A., Moser, D.E. & Spicuzza, M.J. (2014). Hadean age for a post-magmaocean zircon confirmed by atom-probe tomography. natgeosci 7(3), 219–223.

Valley, J.W., Cavosie, A.J., Ushikubo, T., Reinhard, D.A., Lawrence, D.F., Larson, D.J., Clifton, P.H., Kelly, T.F., Wilde, S.A., Moser, D.E., Spicuzza, M.J., 2014. Hadean age for a postmagma- ocean zircon confirmed by atom-probe tomography. *Nat. Geosci.* 7 (3), 219–223.

Van Achterbergh, E., Ryan, C.G., Jackson, S.E. Griffin, W. 2001. Data reduction software for LAICPMS. In Sylvester, P., ed. *Laser ablation ICPMS in the earth sciences: principles and applications*. Mineralogical Association of Canada Short Course Ser. 29, 239-243.

von Quadt, A., Ferrario, A., Diella, V., Hansmann, W., Vavra, G., Köppel, V., 1993. U–Pb ages of zircons from chromitites of the phlogopite peridotite of Finero, Ivrea Zone, N-Italy. *Schweizerische Mineralogische und Petrographische Mitteilungen* 73, 137–138.

Wayne, D. M., and Sinha, K. 1988. Physical and chemical response of zircons to deformation. *Contrib. Mineral. Petrol.* 98:109–121.

Wiedenbeck, M., Allé, P., Corfu, F., Griffin, W.L., Meier M., Oberli, F., Von Quadt, A., Roddick, J.C. Spiegel, W., 1995. Three natural zircon standards for U–Th–Pb, Lu–Hf, trace elements and REE analyses. *Geostandards Newsletter* 19, 1-23.

Woodhead, J.D., Hergt, J.M., 2005. Preliminary appraisal of seven natural zircon reference materials for in situ Hf isotope determination. *Geostandards and Geoanalytical Research* 29, 183–195.

Wu, F.Y., Yang, Y.H., Xie, L.W., Yang, J.H., Xu, P., 2006. Hf isotopic compositions of the 1005 standard zircons and baddeleyites used in U–Pb geochronology. *Chemical Geology* 234, 105-126.

Zanetti, A., Mazzucchelli, M., Sinigoi, S., Giovanardi, T., Peressini, G., Fanning, M., 2013. SHRIMP U–Pb zircon Triassic intrusion age of Finero Mafic Complex (Ivrea–Verbano Zone, Western Alps) and its geodynamic implications. *Journal of Petrology*, 54, 2235–2265.

Zanetti, A., Giovanardi, T., Langone A., Tiepolo M., Wu F.Y., Dallai L., Mazzucchelli, M., 2016. Origin and age of zircon-bearing chromitite layers from the Finero phlogopite peridotite (Ivrea-Verbano Zone, Western Alps) and geodynamic consequences. *Lithos* 262, 58-74.

Figure captions

Figure 1. A) Sketch map of the northeastern sector of the Ivrea-Verbano Zone (westernmost part of the southern Alps) modified after Steck & Tièche (1976) showing the location of dykes/pegmatites studied in this work (white star) and reported in previous work (black stars). B) Geological sketch map of the studied area, SW of the Finero village (Val Cannobina), showing the sample locations (see above for description) and the average attitudes of the different lithologies. Black stars roughly indicate the location of dykes/pegmatites studied in previous works.

Figure 2. A) Photograph of the outcrop showing one of the studied dyke (ALB samples) intruded in metadiorites. The dyke is cut by later faults highlighted in picture as dotted white lines. B) Detail of A showing the highly deformed appearance of the dykes and the

main mineral assemblage consisting of plagioclase and biotite (dark layers). C) photograph of a smaller dyke (7cm thick) showing the sharp contact with the host metadiorites. D) Equal area projection (lower hemisphere) of dyke attitudes studied in this work and reported by Stähle et al., (1990) and of the foliation planes (poles) of the host metadiorites. E) scan of the ALB-1A_mp thin section showing the main textural features and location of analysed zircon grains. Mineral abbreviation after Kretz (1983).

Figure 3. A) microphotograph showing plagioclase occurring as porphyroclasts and fine-grained recrystallized matrix. B) microphotograph of the mafic layer consisting of biotite and zoisite. C) microphotograph of a rounded corundum grain embedded in fine grained matrix (recrystallized plagioclase) showing numerous fractures. D) SEM-BSE image of euhedral corundum grains surrounded by oxides (both magnetite and spinel). The image shows also the local occurrence of K-feldspar within the matrix. E) Photograph of a large (cm-sized) corundum grain surrounded by plagioclase+oxides. Mineral abbreviation after Kretz (1983).

Figure 4. A) Microphotograph of the mylonitic matrix with an elongated monazite grain (60x25 μm). B) SEM-BSE image of the monazite grains showing the compositional zoning consisting of with a central brighter Th-rich area surrounded by darker lower Th domain (see Table 1 for analyses). C) Stereomicroscopic picture of a zircon fragments surrounded by recrystallized plagioclase. Zircon fragments are fractured with local displacement. Biotite and spinels define a pressure shadow. The orientation of the mylonitic foliation (Sm) is also shown. D) BSE images showing zircon grains partially aligned with respect to the mylonitic foliation (Sm). Zircon grains are fractured and some of the fractures are aligned parallel to the foliation. E) microphotograph of zircon aggregate consisting of a

large subhedral grains showing numerous fractures arranged in two main sets one of which is oriented parallel to the mylonitic foliation (Sm). F) Anhedral zircon grains highly fractured and surrounded by spinels.

Figure 5. A) SEM-CL image of an almost homogeneous zircon grain (Zrc5, ALB-1A) with a narrow darker rim on one side. Fractures are abundant, one on them is large, filled by spinels and separates two slightly displaced fragments. CL mosaic textures are well recognizable. B) CL image of Zrc2 from sample ALB-1A showing sector zoning, fractures and CL mosaic textures. C) CL image of subhedral zircon grains (Zrc1, 3, 4 from ALB-1A sample) showing domains with different CL properties, fractures and CL mosaic textures. Details of the textural site are shown in Fig. 5D. D)-E) CL image of zircon grains Zrc3 and Zrc2 from ALB-1A_mp showing complex zoning features: oscillatory, sector and broad-band zoning overprinted by mosaic textures as well as fractures. See Fig. 3A for textural localization. Both CL images contain artefacts (brighter horizontal bands) resulting from stitching several smaller CL images.

The orientation of the mylonitic foliation (Sm) is also shown in each picture.

Figure 6. A) CL images of an aggregate of zircon fragments (Zrc1 ALB-1B_mp) resulting from the stitching of several smaller images. The CL image contains artefacts (brighter horizontal bands) resulting from stitching process. Sector, oscillatory and broad-band zoning are overprinted by mosaic-like textures. Fractures are abundant and partly oriented parallel to the mylonitic foliation (Sm). The space among fragments is generally filled by spinels and biotite. B) detail of A) showing the oscillatory zoning in two main adjacent fragments. Several small fragments with lobate contours are visible in between. Highly sheared zones are also visible. C) Detail of A) showing the effect of shearing consisting mainly of veining and fracturing. Dark small areas represent void/inclusions.

Figure 7. A) CL image and B) EBSD mapping of Zrc1 from ALB-1A_mp sample. C) and E) show 2 details (white boxes in B) mapped by EBSD at 1 μm steps; D) and F) are the local disorientation gradient map showing maximum disorientation of about 2.5° of the mosaic texture.

Figure 8. A) Left: Orientation map for a fragment of Zrc1 from sample ALB-1B_mp (see CL images in Fig. 5) showing disorientation relative to the average orientation of the whole grain (ϕ_1 , θ , ϕ_2 : 135.63, 160.06, 74.62). Note the occurrence of domains with similar disorientation of ca. 5° in the interior and at the edges of the crystal. Right: lower hemisphere equal area plot depicting the average orientation of some low index crystallography directions (as poles normal to planes) in the sample reference frame. The c-axis is approximately lying normal to the surface (i.e. parallel to the Z-direction of the stage). B) Enlargement of A) highlighting the only part of the crystal (left side) that shows gradual changes in orientation related to indentation/fragmentation. Note change in the scale of the colour bar relative to A). C) Local disorientation gradient map showing maximum disorientation of about 2° of the mosaic texture. Smaller angles corresponding to rotations of about 0.5° are also observed. Note gradual disorientations related to the indentation/fragmentation. The profile a-a' showing relative and absolute disorientations is reported in Fig. A.2. D) SEM-CL image of zircon domain (left side) that shows gradual changes in orientation related to indentation/fragmentation. E) Lower hemisphere equal area pole figures of (a) area A and (b) area B, showing the dispersion of the orientation of

some low index crystallography directions. Disorientation axes of small angles in the sample and crystal reference frame are also shown.

Figure 9. A) and C) plots of $^{206}\text{Pb}/^{238}\text{U}$ and U-Pb concordant data for Zrc4 and Zrc2 from ALB-1A thin section. B) and D) contour maps of $^{206}\text{Pb}/^{238}\text{U}$ data superposed on the CL images. The transparent white areas delimit $^{206}\text{Pb}/^{238}\text{U}$ data younger than 240 Ma, the spots positions (black filled circles) yielding U-Pb concordant data (Ma, black numbers within white boxes) are also shown.

Figure 10. A), B) and C) plots of $^{206}\text{Pb}/^{238}\text{U}$ and U-Pb concordant data for Zrc2 and Zrc3 from ALB-1A_mp thin section and Zrc1 from ALB-1B_mp thin section. B), D), and F) CL images of Zrc2 and Zrc3 from ALB-1A_mp thin section and Zrc1 from ALB-1B_mp thin section with location of LA-ICP-MS and LA-MS-ICP-MS analytical spots.

Figure 11. A) CL image of Zrc4 (ALB-1A) showing the position of LA-ICP-MS spots (50 μm) used for trace elements analyses. Spots are subdivided in two main groups, black and white circles. The latter can be filled in white and black representing maxima of some trace element (see text for more details). The letters on the left represent the raw labels, numbering (from 1 to n) reported in Table A2 starts from the left. B) and C) Contours maps of Y and U concentrations (ppm), respectively. D) and E) Y vs Th/U ratio and U/Yb ratio vs Hf plots, symbols within the plots are coherent with those reported on CL images A) and F). F) CL image of Zrc2 (ALB-1A) showing the position of LA-ICP-MS spots (50 μm) collected along two profiles, i.e. parallel (white filled squares) and at high angle (black filled squares) with respect to the foliation planes.

Figure 12. A) Y vs Th/U ratio plot, B) U/Yb ratio vs Hf plot and C) $\xi\text{Hf}(0)$ values for Zrc2 and Zrc3 from ALB-1A_mp sample and Zrc1 from ALB-1B_mp sample.

Figure 13. A) C1 chondrite normalized REE patterns of different chemical domains of Zrc4 (ALB-1A): average values of (a) the darkest CL band showing highest Nb, Ce, Ta, Pb, Th, U and HREE concentrations, (b) the dark CL domain and (c) the brighter CL domains. The grey area delimits C1 chondrite normalized REE patterns of megacrystic zircon in nepheline pegmatites of the IVZ from Schaltegger et al. (2015). B) transparent area delimits C1 chondrite normalized REE patterns for Zrc2 (ALB-1A). C), D) and E) C1 chondrite normalized REE patterns of different domains of Zrc2 (ALB-1A_mp), Zrc3 (ALB-1A_mp) and Zrc1 (ALB-1B_mp), respectively. Normalization values are from McDonough and Sun (1995).

Figure 14. Schematic reconstruction of the microstructural evolution of zircon (Zrc1) within the dyke. A) Dyke emplacement with crystallization of the main mineral assemblage: plagioclase, zircon and corundum. B) Metasomatic event leading to the formation of biotite+spinel rich (melanocratic) layers and crystallization of new zircon grains. In this stage, Zrc1 experienced deformation with partial/total U-Pb resetting and trace elements variations. C) Ductile deformation of both leucocratic and melanocratic layers with local recrystallization of zircon and formation of syn-kinematic monazite.

Figure 15. U-Pb zircon data from this work and available from the literatures relative to the lower crustal magmatic history of the northern sector of the IVZ are plotted on a time diagram, from Late Carboniferous (C.) to Jurassic. References: (a) Zanetti et al. (2013); (b) Grieco et al. (2001); (c) Schaltegger et al. (2015); (d) Oppizzi & Schaltegger (1999); Stähle et al. (1990); Badanina & Malitch (2012); (g) Zanetti et al. (2016).

Figure A.1. A) Thin section scan of the meta-diorite sample (M20) hosting the (ALB) dyke showing the porphyroclastic textures and the ultramafic lens. The white boxes delimit the areas studied in more detail at the SEM and showed in BSE images of B), C), and D). B) BSE image of a Cpx porphyroclast with Amph-2 overgrowth. C) BSE image of different generations of amphibole plagioclase. D) BSE image of the mineral assemblage of the ultramafic lens. Mineral abbreviation after Kretz (1983).

Figure A.2. Profile a-a' in Fig. 8C showing relative and absolute disorientations. Bottom is an enlargement of Fig. 8C highlighting the correlation between the local disorientations and the map (arrows). Continuous line in the absolute disorientation profile shows the measurement noise of about 0.2°.

Table captions

Table 1. EMPA analyses of dyke-forming minerals. Two analyses of different BSE domains of a monazite grain are also reported.

Table 2. List of studied zircon grains and adopted techniques.

Table A1. LA-ICP-MS isotopic data of zircon and monazite.

Table A2. LA-ICP-MS trace element composition of zircon grains.

Table A3. LA-MC-ICP-MS Hf isotopic results of zircon

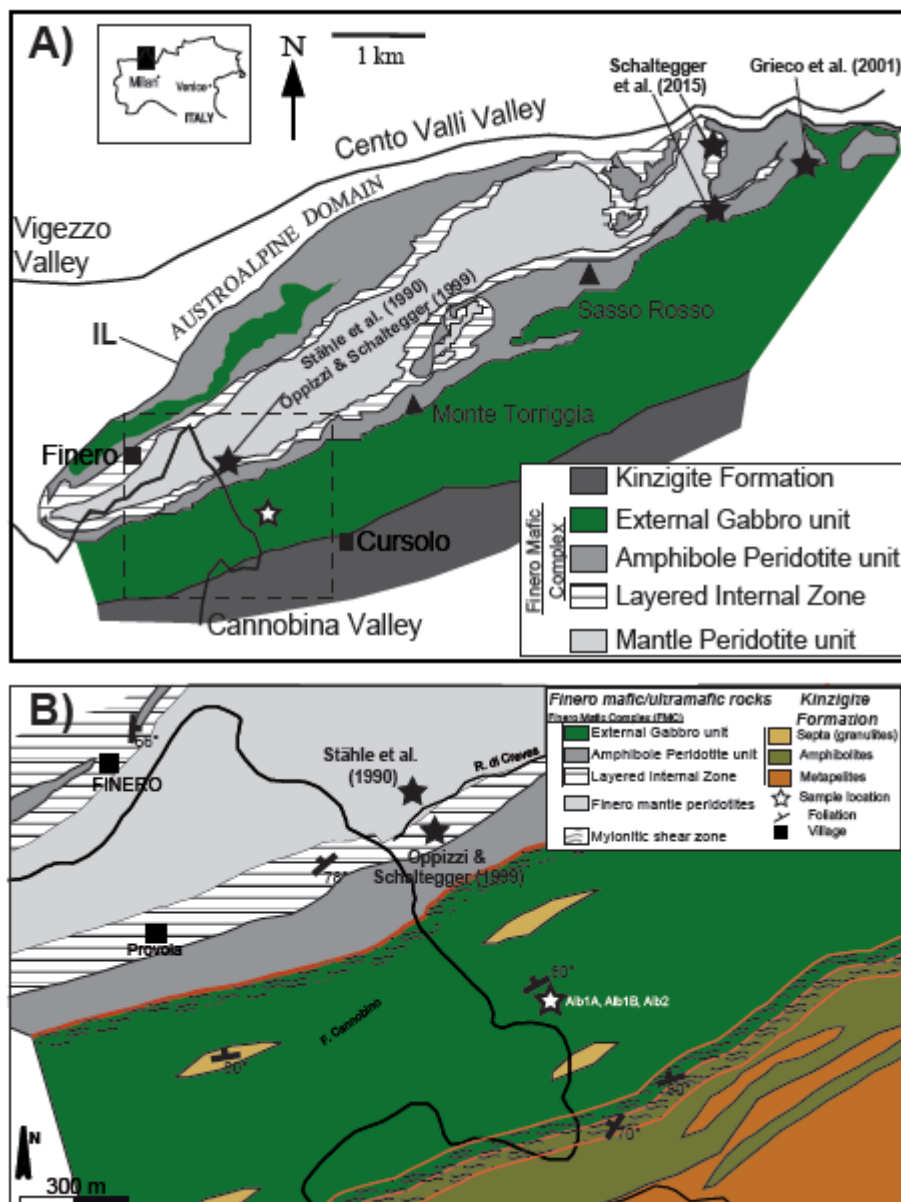


Figure 1

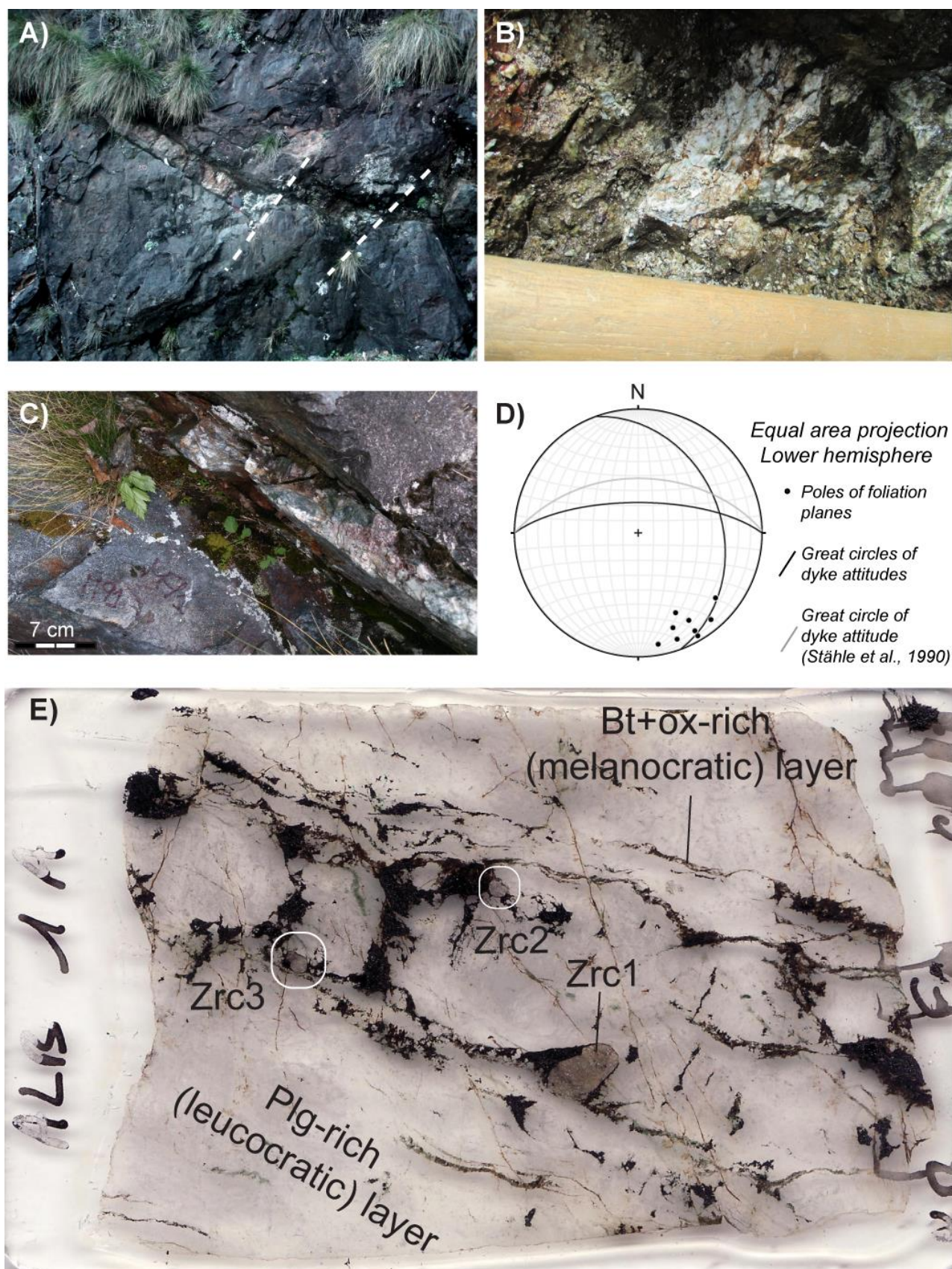


Figure 2

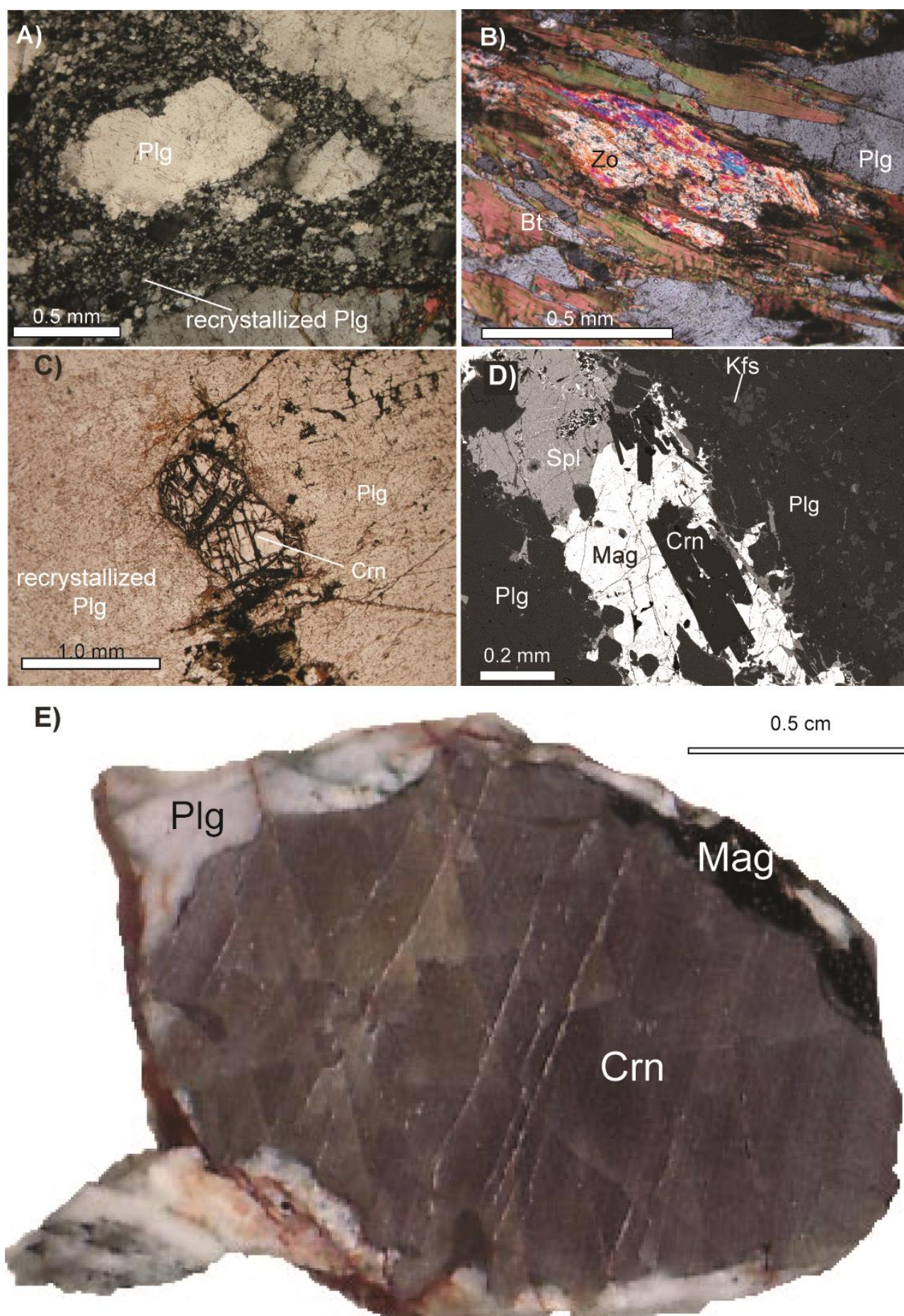


Figure 3

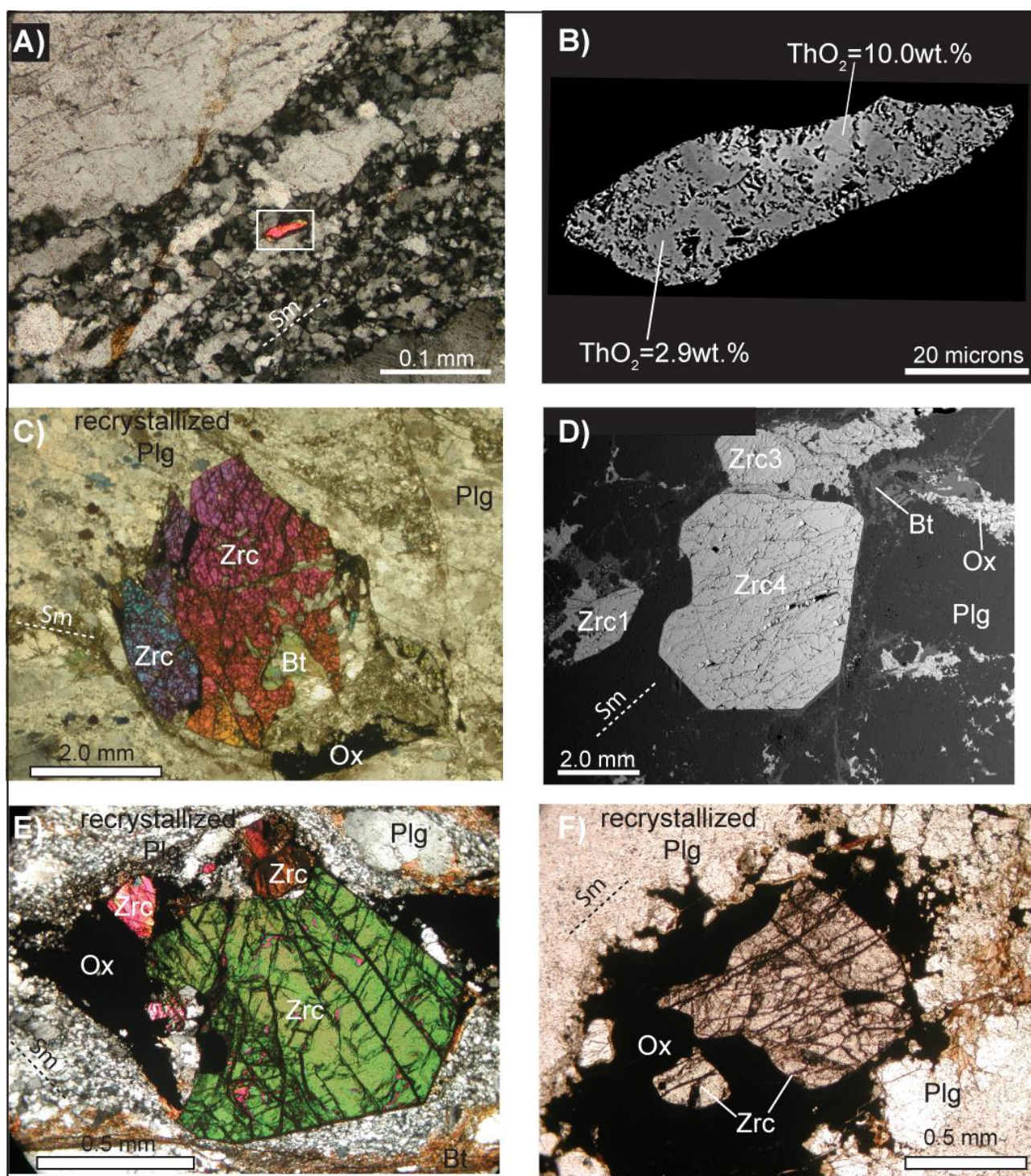
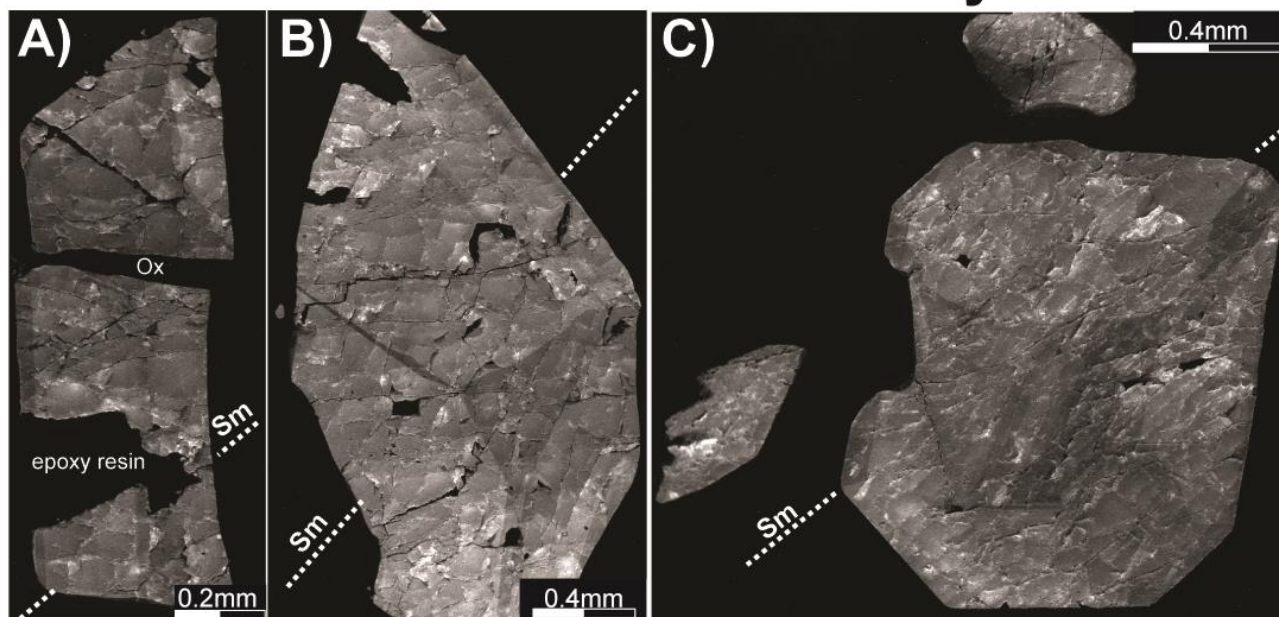


Figure 4

Zircon from leucocratic layers



Zircon from melanocratic layers

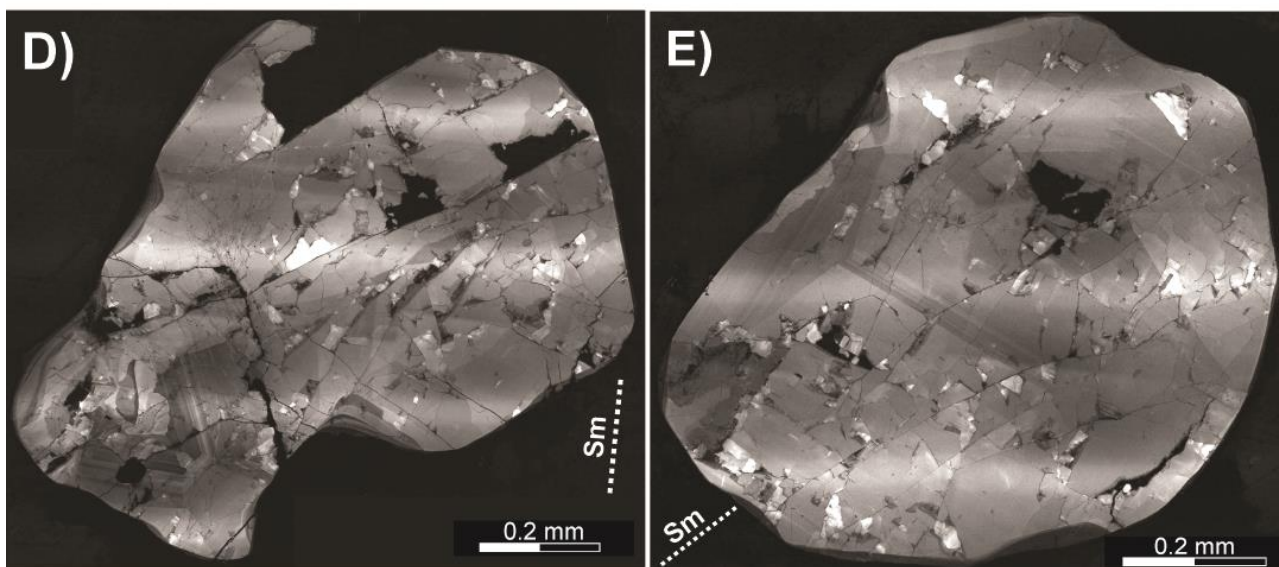


Figure 5

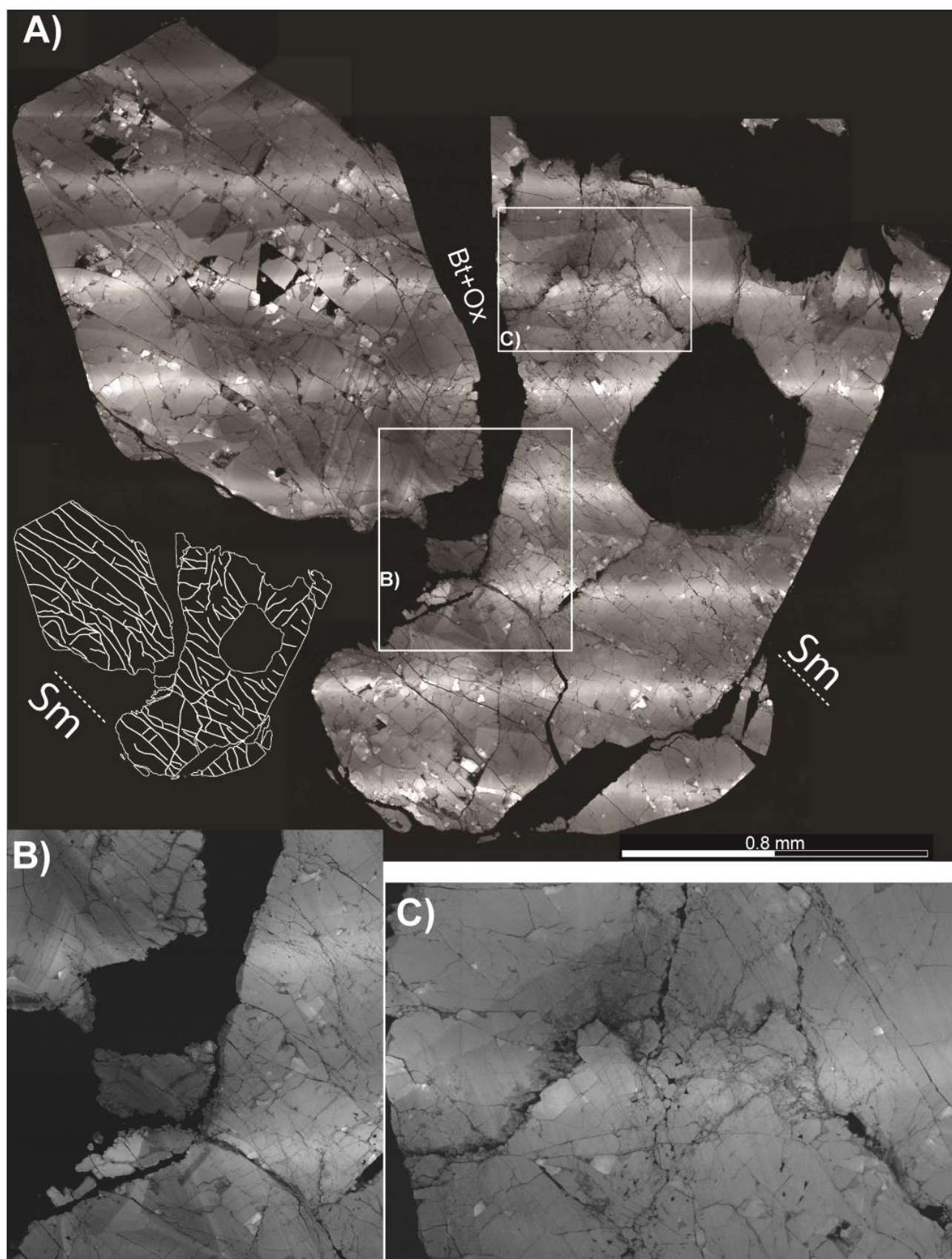


Figure 6

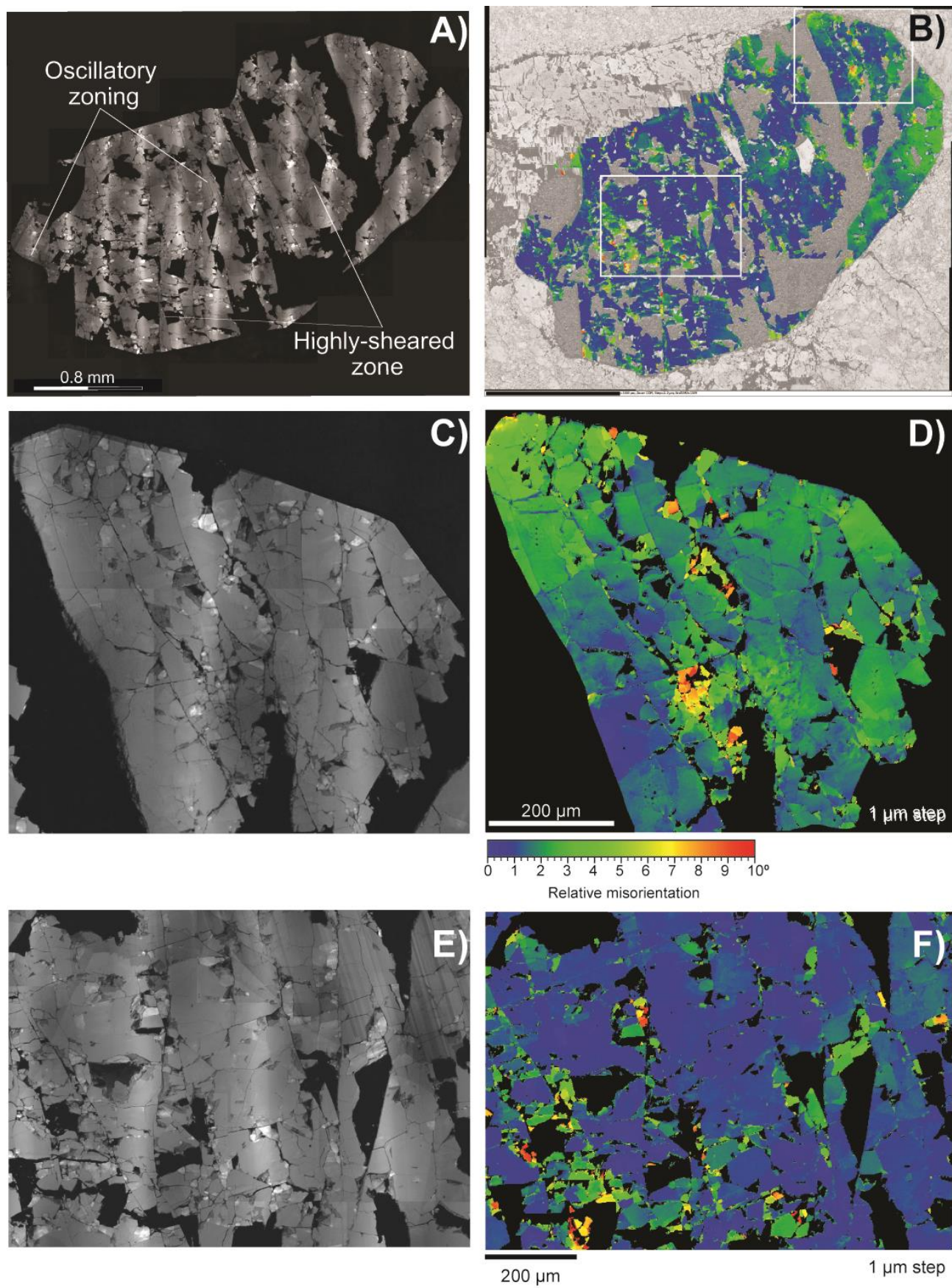


Figure 7

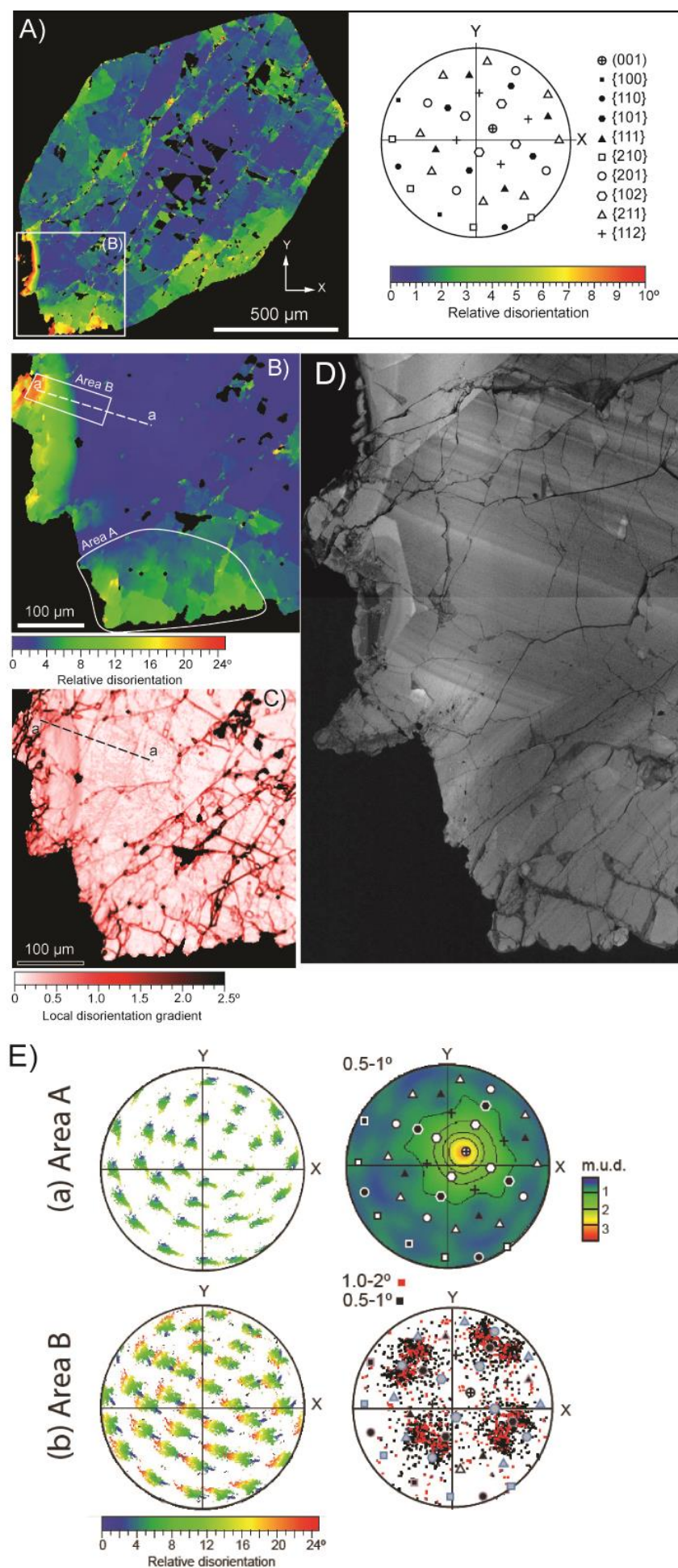


Figure 8

ACCEPTED MANUSCRIPT

Zircon from leucocratic layers

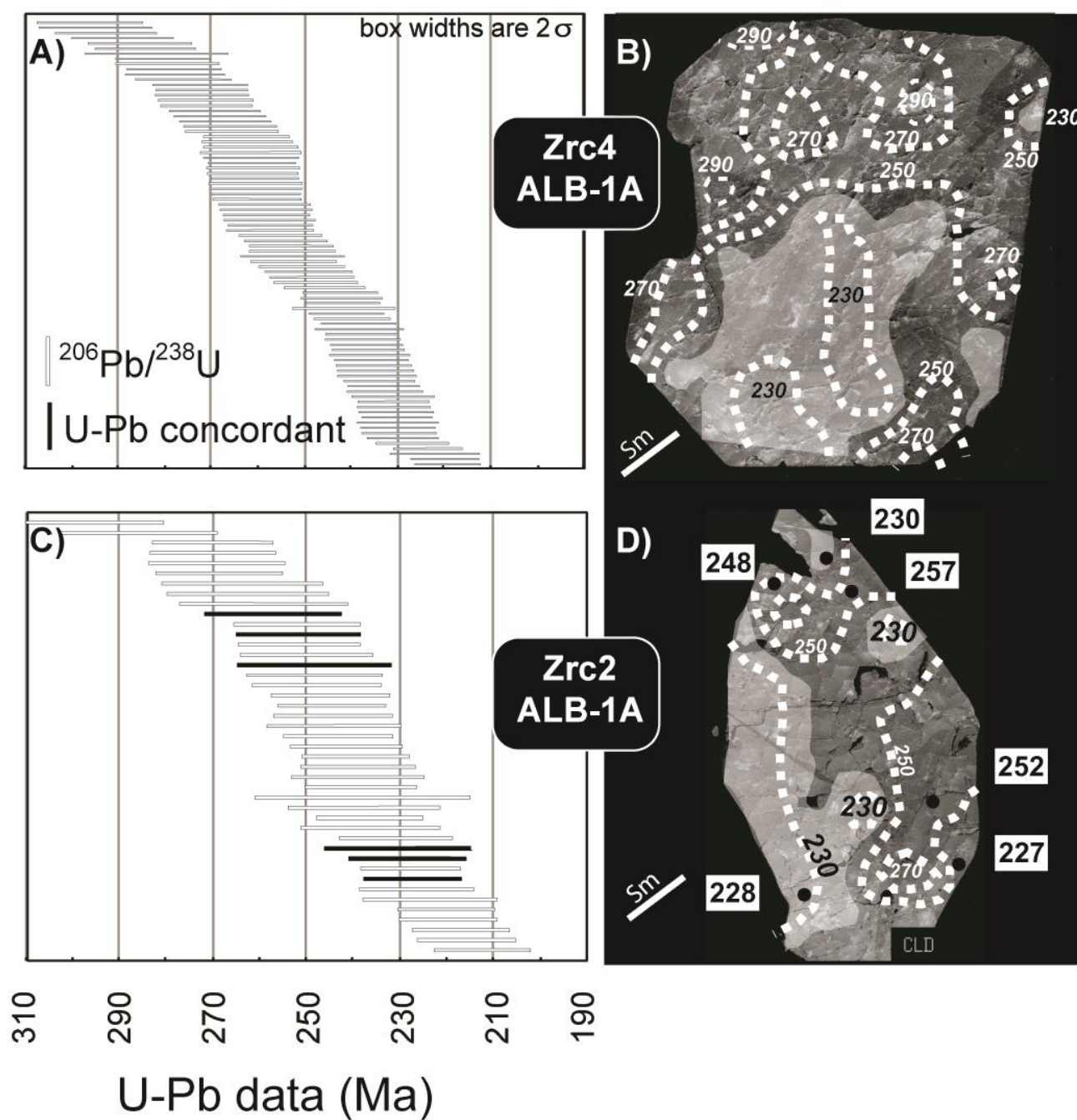


Figure 9

Zircon from melanocratic layers

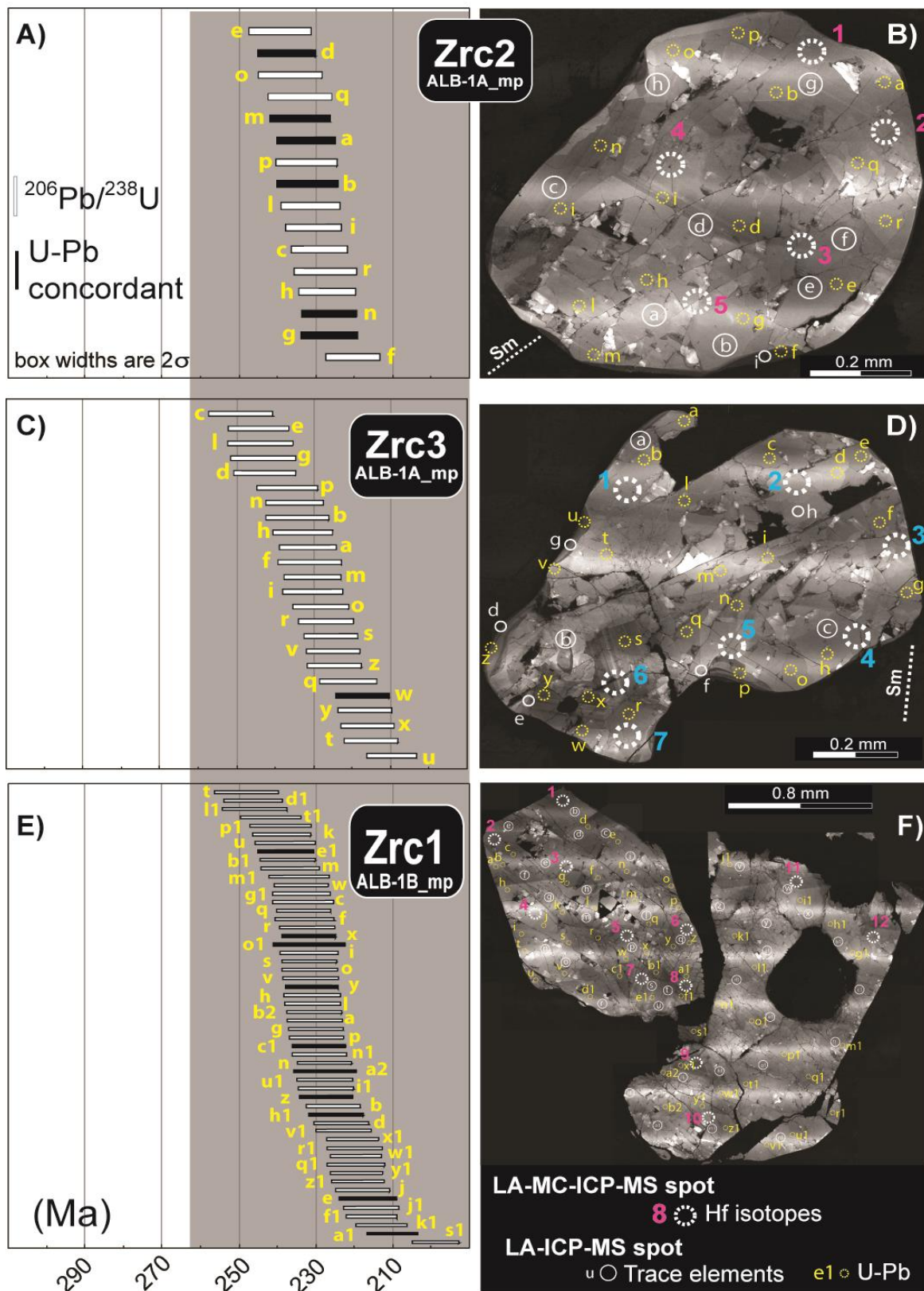


Figure 10

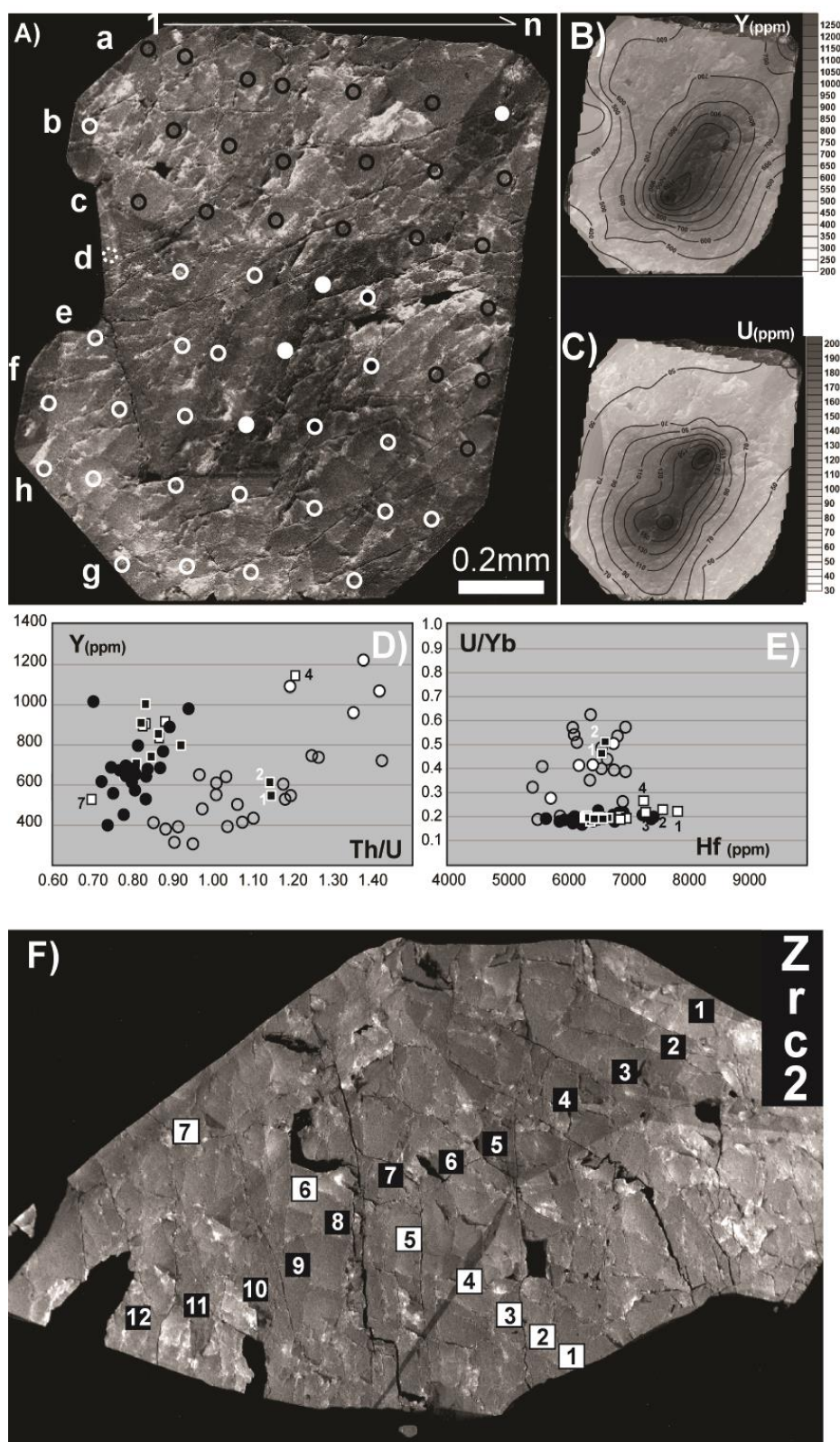


Figure 11

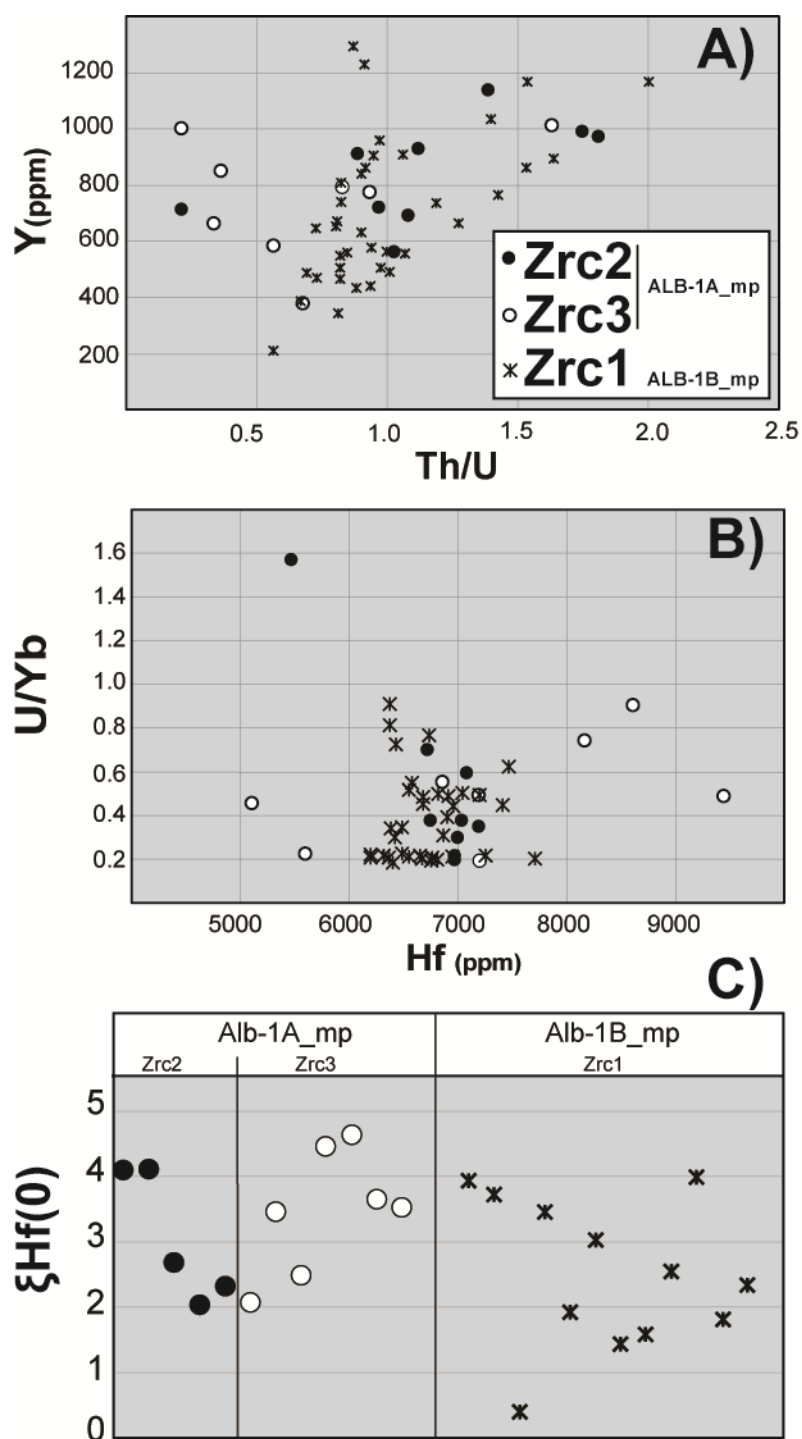


Figure 12

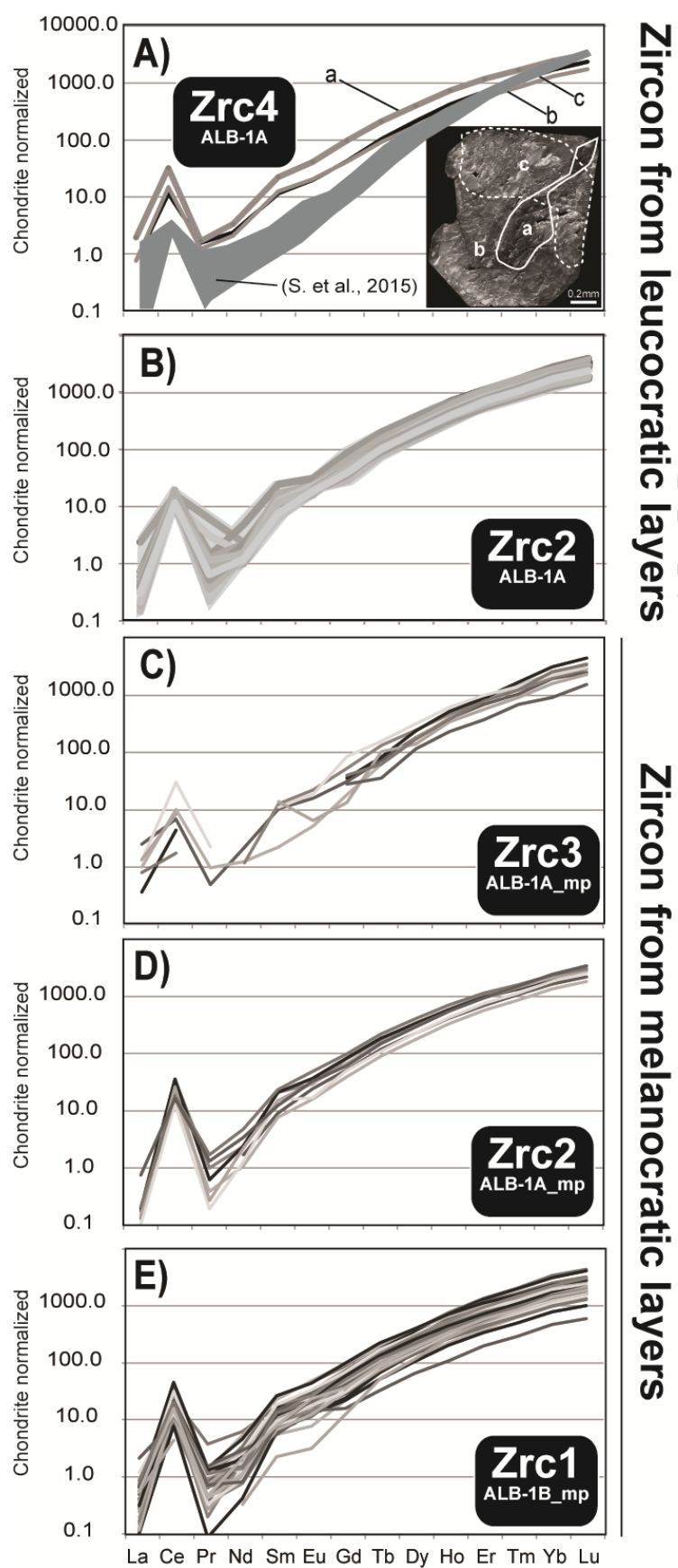


Figure 13

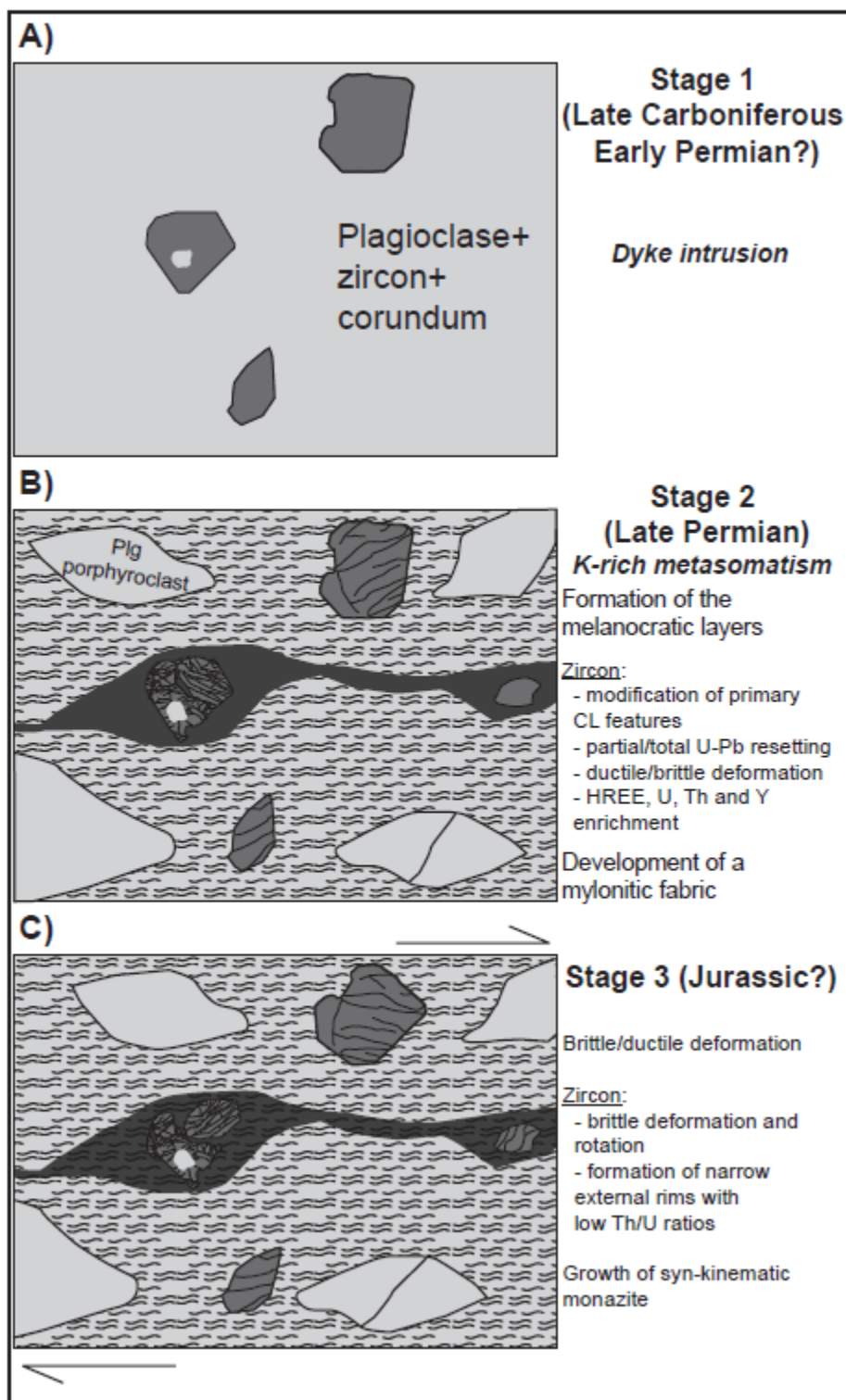


Figure 14

Magmatic events within the northern sector of the IVZ

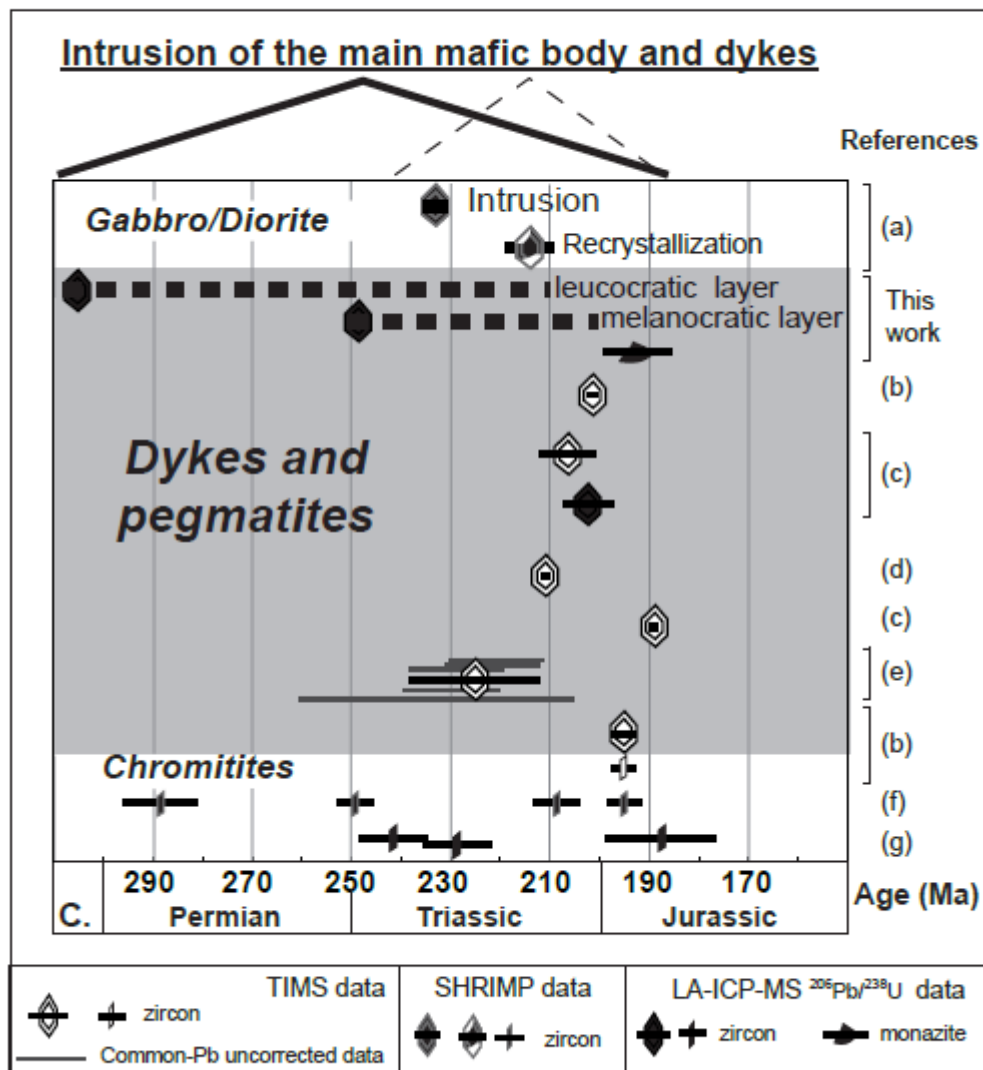
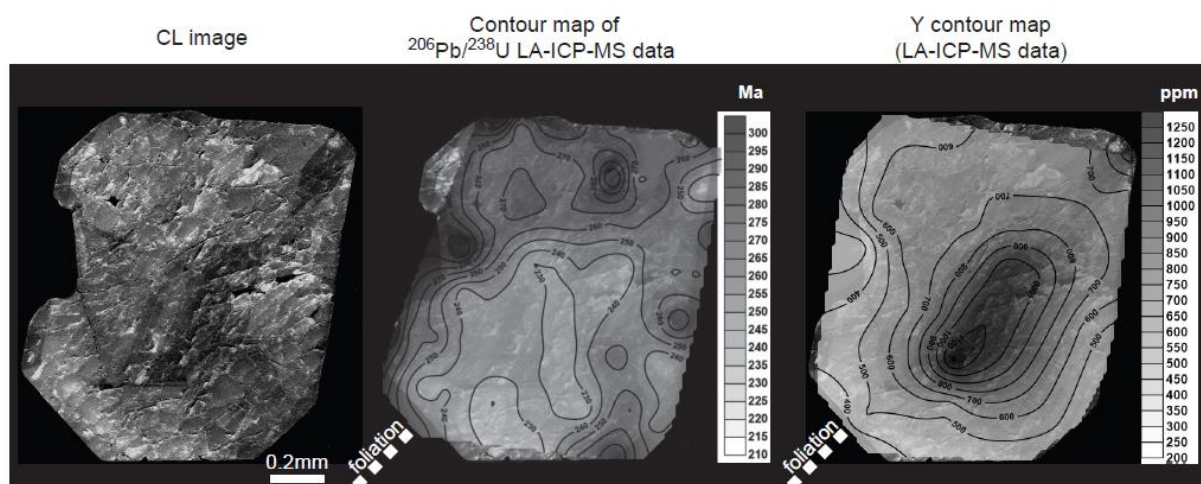


Figure 15



Graphical abstract

Table 1

Thin section	Grain#	Dimensions (mm)	SEM		LA-ICP-MS analyses (n.; spots size)		LA-MC-ICP-MS (n.; spots size)
			CL	EBS	U-Pb	Trace element	Hf isotopes
ALB-1A	Zrc2	1.2x0.7	X		(43; 35µm)	(19; 50µm)	
	Zrc4	1.2x0.8	X		(84; 35µm)	(50; 50µm)	
ALB-1B							
ALB-2	Mnz1	0.07x0.02			(3, 10µm)		
ALB-2_mp							
ALB-1A_mp	Zrc1	3.2x1.6	X	X			
	Zrc2	0.9x0.7	X		(15; 35µm)	(9; 50µm)	(5; 65µm)
	Zrc3	1.0x0.7	X		(24; 35µm)	(8; 50µm)	(7; 65µm)
ALB-1B_mp	Zrc1a	1.5x0.9	X	X	(32; 35µm)	(19; 50µm)	(8; 65µm)
	Zrc1b	1.7x0.8	X		(22; 35µm)	(18; 50µm)	(4; 65µm)

Table 2

No.	1	14	9	1	11	2		1	2
Sample	Alb1A	ALB2	ALB2	ALB2	ALB2	ALB1B		ALB2	ALB2
Mineral	Plg	Kfs	Bt	Zo	Spl	Spl*		Mnz	Mnz
Comment								BSE	BSE
								bright	dark
SiO2	64.29	67.00	35.66	45.42	0.04	0.57	SiO2	0.72	0.05
TiO2	0.02	0.00	1.79	0.00	0.05		P2O5	27.98	28.61
Al2O3	21.44	18.83	18.37	24.67	59.33	55.61	Pr2O3	2.88	3.17
Cr2O3	0.02	0.00	0.00	0.00	0.02		CaO	1.92	0.80
FeO	0.02	0.00	20.96	0.16	34.97	28.96	Y2O3	3.69	4.21
MnO	0.01	0.00	0.26	0.00	3.51	1.59	La2O3	11.75	13.89
NiO		0.00	0.06	0.01	0.05		Nd2O3	8.46	10.34
MgO	0.03	0.00	10.05	0.00	3.61	7.15	UO2	0.81	0.54
CaO	3.77	0.04	0.13	25.36	0.00	0.01	Ce2O3	24.57	28.50
Na2O	9.63	0.86	0.09	0.02	0.04	1.00	Sm2O3	1.64	2.01
K2O	0.05	15.25	9.71	0.00	0.01		ThO2	10.05	2.88
ZnO						5.12	Eu2O3	0.00	0.00
							Gd2O3	1.29	1.44
Total	99.28	101.99	97.09	95.64	101.64	94.88	Total	95.76	96.45
An	17.7	0.2							
Ab	82.0	7.9							
Or	0.3	91.9							

Ductile-brittle deformation effects on crystal-chemistry and U-Pb ages of magmatic and metasomatic zircons from a dike of the Finero Mafic Complex (Ivrea-Verbano Zone, by Langone A. et al.

Highlights

- Millimetre-size zircon grains were observed in dioritic dykes.
- Dykes experienced a subsequent metasomatism with zircon crystallization/annealing.
- U-Pb ages and REE distributions within zircon grains are related to microstructures.